



1 **Measurement report: Intensive biomass burning emissions and**
2 **rapid nitrate formation drive severe haze formation in Sichuan**
3 **basin, China: insights from aerosol mass spectrometry**

4 Zhier Bao¹, Xinyi Zhang¹, Qing Li¹, Jiawei Zhou¹, Guangming Shi², Li Zhou², Fumo Yang²,
5 Shaodong Xie³, Dan Zhang⁴, Chongzhi Zhai⁴, Zhenliang Li⁴, Chao Peng⁴, and Yang Chen¹

6 ¹ Chongqing Institute of Green and Intelligent Technology, Chinese Academy of Sciences,
7 Chongqing, 400714, China

8 ² Department of Environmental Science and Engineering, College of Architecture and Environment,
9 Sichuan University, Chengdu 610065, China

10 ³ SKL-ESPC and BIC-ESAT, College of Environmental Sciences and Engineering, Peking
11 University, Beijing 100871, China

12 ⁴ Academy of Environmental Science, Chongqing, 401147, China

13

14 Correspondence: Yang Chen (chenyang@cigit.ac.cn)

15 **Abstract**

16 Haze pollution is a severe environmental problem, caused by elevation of fine particles
17 (aerodynamic diameter < 2.5 μm, PM_{2.5}), which is related to secondary aerosol formation,
18 unfavourable synoptic conditions, regional transport, etc. The regional haze formation in basin areas,
19 along with intensive emission of precursors, high relative humidity and poor dispersion conditions,
20 is still limitedly understood. In this study, a field campaign was conducted to investigate the factors
21 resulting in haze formation in Sichuan Basin (SCB) during winter in 2021. The fine aerosol chemical
22 composition was characterised by using a time-of-flight aerosol chemical speciation monitor (ToF-
23 ACSM) with the aim of inorganic and organic aerosol characterisation and source apportionment.
24 The average concentration of non-refractory fine particles (NR-PM_{2.5}) was 98.5 ± 38.7 μg/m³, and
25 organics aerosols (OA), nitrate, sulphate, ammonium, and chloride occupied 40.3, 28.8, 10.6, 15.3
26 and 5.1 % of PM_{2.5}. Three factors, including a hydrocarbon-like OA (HOA), a biomass burning OA
27 (BBOA), and an oxygenated OA (OOA), were identified by applying the positive matrix



28 factorisation (PMF) analysis, and they constituted 24.2, 24.2 and 51.6 % of OA on average,
29 respectively. Nitrate formation was promoted by gas-phase and aqueous-phase oxidation, while
30 sulphate was mainly formed through aqueous-phase. OOA showed strong dependence on Ox,
31 demonstrating the contribution of photooxidation to OOA formation. OOA concentration increased
32 as aerosol liquid water content (ALWC) increased within $200 \mu\text{g}/\text{m}^3$ and kept relatively constant
33 when $\text{ALWC} > 200 \mu\text{g}/\text{m}^3$, suggesting the insignificant effect of aqueous-phase reactions on OOA
34 formation. Among the three haze episodes identified during the whole campaign, the driving factors
35 were different: the first haze episode (H1) was driven by nitrate formation through photochemical
36 and aqueous-phase reactions, and the second haze episode (H2) was mainly driven by the intense
37 emission of primary organic aerosols from biomass burning and vehicle exhaust, while the third
38 haze episode (H3) was mainly driven by reactions involving nitrate formation and biomass burning
39 emission. HOA and BBOA were scavenged, while OOA, nitrate, and sulphate formation were
40 enhanced by aqueous-phase reactions during fog periods, which resulted in the increase of O:C from
41 pre-fog to post-fog periods. This study revealed the factors driving severe haze formation in SCB,
42 and implied the benefit of controlling nitrate as well as intense biomass burning and vehicle exhaust
43 emission to the mitigation of heavy aerosol pollution in this region.

44
45
46



47 1. Introduction

48 Although a series of emission reduction strategies had been implemented to mitigate severe
49 haze pollution over a decade in China, the fine particle (particulate matter with aerodynamic
50 diameter less than 2.5 μm , $\text{PM}_{2.5}$) pollution events still occurred, especially during autumn and
51 winter (Ding et al., 2019; Zhao et al., 2020; Yan et al., 2020). Haze formation was affected by the
52 intense emission of primary particles, rapid formation of secondary aerosols, stagnant
53 meteorological conditions, and topography. The interplay among these factors usually makes haze
54 formation complex (Bao et al., 2019; Guo et al., 2014; Zheng et al., 2015), which resulted in
55 difficulties in making air pollution mitigation strategies.

56 Many studies showed that the rapid increase of secondary aerosols (including secondary
57 inorganic/organic aerosols, i.e., SIA and SOA) played an important role in haze formation (Huang
58 et al., 2014; Wu et al., 2022). Nitrate, sulphate, and ammonium, mainly formed through
59 photochemical oxidation and aqueous-phase reactions in the atmosphere, were the major component
60 of SIA. Previous studies demonstrated that the substantial formation of nitrate and sulphate
61 exacerbated severe haze development (Wang et al., 2020; Liu et al., 2020). For example, (Zheng et
62 al., 2016) investigated the factors driving haze formation in Beijing in 2013, and the results showed
63 that the enhanced production of sulphate and nitrate led to their increased contribution to $\text{PM}_{2.5}$ as
64 the pollution level increased, while the contribution of organic matter (OM) decreased. The emission
65 of SO_2 had been reduced dramatically over the past ten years in China; however, NO_x did not show
66 a significant reduction. Thus, the haze formation was found to be mainly driven by the reactions
67 generating nitrate in recent years (Fu et al., 2020; Li et al., 2018; Zhou et al., 2021; Zhai et al., 2021).

68 Compared to SIA, the formation process of SOA was more complicated (Chen et al., 2017).
69 SOA could be formed through the gas-phase photooxidation of volatile organic compounds (VOCs),
70 which was affected by temperature, relative humidity (RH), and total organic aerosol mass loadings
71 (Clark et al., 2016; Hinks et al., 2018; Donahue et al., 2006). SOA could also be formed through the
72 oxidation of water-soluble VOCs or organic products of gas-phase photochemistry, which was
73 observed in the field and laboratory studies (Liu et al., 2018; Chen et al., 2015). Besides, the aging
74 of primary organic aerosols (POA) by oxidants in the atmosphere also contributed to SOA (Wang
75 et al., 2021; Gilardoni et al., 2016). For instance, the organic aerosols emitted from biomass burning



76 were oxidised through the photochemical oxidation process driven by OH radicals which might take
77 place in both gas and aqueous phases (Paglione et al., 2020). The variations of regional and seasonal
78 emissions might also affect the formation of SOA (Dai et al., 2019; Sun et al., 2016). Thus, it is of
79 vital importance to consider various factors when investigating SOA formation.

80 Similar to the city clusters such as Beijing, Shanghai and Guangzhou in North China Plain
81 (NCP), Yangtze River Delta (YRD) and Pearl River Delta (PRD), the Chengdu-Chongqing city
82 cluster, located in the Sichuan Basin (SCB) in Southwest China, was also suffering severe haze
83 pollution (Tao et al., 2017; Tan et al., 2019). Many efforts had been made to investigate the temporal
84 variation, chemical composition and formation mechanism of PM_{2.5} during the evolution of haze
85 episodes in NCP, YRD and PRD (Peng et al., 2021; Sun et al., 2016; Zhang et al., 2015; Yan et al.,
86 2020), whereas, only a few studies focused on the factors resulting in haze formation in SCB (Zhang
87 et al., 2019; Song et al., 2019). These studies mainly focused on the formation of inorganic species
88 in PM_{2.5}, and the results showed that the rapid formation of SIA under high RH conditions promoted
89 the increase of PM_{2.5}. However, further studies on the characteristics of OA, including the temporal
90 evolution, sources and formation pathways, were still lacking.

91 The area of SCB is ~260,000 km² and its population is ~110 million, making it an important
92 developing region in Southwest China. The basin is a subtropical expanse of low hills and plains
93 and is completely encircled by high mountains and plateaus, which is unfavourable for either
94 horizontal transport or vertical diffusion. The atmosphere in SCB was characterised by persistently
95 high relative humidity and low wind speed all year round. The haze evolution in SCB might be
96 different from those in other regions due to its unique topography, meteorological conditions and
97 emission sources, which remained unclear. Therefore, comprehensive studies are needed to reveal
98 the key factors contributing to haze formation in the basin (Wang et al., 2018).

99 The Time-of-Flight Aerosol Chemical Speciation Monitor (ToF-ACSM) is a robust and highly
100 sensitive instrument that provides real-time characterisation and composition of non-refractory
101 PM₁/PM_{2.5} (NR-PM₁/PM_{2.5}) depending on the type of the aerodynamic lens used (Liu et al., 2007;
102 Xu et al., 2017). Compared to the Aerodyne aerosol spectrometer (AMS), the ToF-ACSM is more
103 compact and cheaper. However, the ToF-ACSM does not figure particle sizing. Compared to the
104 quadrupole-ACSM (Q-ACSM), the ToF-ACSM has better mass resolution and detection limits
105 (Fröhlich et al., 2013). Although the ToF-ACSM had not been widely deployed in field observations



106 as AMS/Q-ACSM did in a number of different sites over China, it had successfully characterised
107 the variation of $PM_1/PM_{2.5}$ and the sources of organic aerosols in the cities within NCP, YRD and
108 PRD (Ge et al., 2022; Sun et al., 2020; Guo et al., 2020). Despite this, few studies applied a Q/ToF-
109 ACSM or AMS in SCB. The responses of aerosol chemistry to meteorology and emissions therein
110 remained poorly understood. To the authors' best knowledge, this is the first time that the ToF-
111 ACSM has been deployed in the field observations within SCB.

112 The present study aims to uncover the factors driving severe haze formation during winter in
113 SBC. The characteristics of NR- $PM_{2.5}$, including mass concentration, chemical composition,
114 temporal and diurnal variation, were described in detail. The OA sources resolved by the positive
115 matrix factorisation (PMF) analysis and elemental composition were investigated to elucidate the
116 possible aging process of OA. The formation mechanism for SIA and SOA was also studied based
117 on the dependencies of nitrate, sulphate and OOA with odd oxygen ($O_x = O_3 + NO_2$) and aerosol
118 liquid water content. In addition, the evolution process of chemical composition and elemental
119 composition were summarised during different haze and fog episodes to investigate the main factors
120 exacerbating haze pollution. The data and results would fill the knowledge gap on the factors
121 affecting haze formation in SCB and provide a scientific basis for future air pollutant mitigation
122 strategies in this unique basin.

123 2. Material and methods

124 2.1 Sampling site

125 The field study was carried out from 18 December 2021 to 22 January 2022 at a site (30°55'59"
126 N, 104°12'25"E) in Deyang, and the site was near the northern border of Chengdu, the capital of
127 Sichuan province, China (as shown in Fig. 1). The site was located in a typical suburban region
128 surrounded by several food, aluminium alloy, and building materials factories. There was a main
129 road ~200 m south of the site. The north and west of the site were croplands and villages. Thus, the
130 site was affected by traffic emissions, biomass burning and industrial pollutants. The study at this
131 site would help to understand the characteristics of regional haze pollution and the influence of
132 regional transport between urban and suburban areas on haze formation



133 2.2 Instrumentation

134 During the campaign, the mass loadings of non-refractory organics, nitrate, sulphate,
135 ammonium and chloride in $PM_{2.5}$ were obtained online by a ToF-ACSM. The gaseous species,
136 including NO, NO₂, O₃, SO₂, CO and CO₂, were continuously measured by the Thermo gas
137 analysers (model 43i, 49i, 42i, 48i and 410i). The meteorological parameters, including temperature
138 (T), relative humidity (RH), solar radiation (SR), wind speed (WS) and wind direction (WD), were
139 obtained by an automatic weather station (Luff WS501-UMB).

140 For the NR- $PM_{2.5}$ measurement, the ambient air was pumped into the sampling line via a
141 vacuum pump, and the flow rate was maintained at 3 L/min with a flow meter. Before being sampled
142 by the ToF-ACSM, the ambient air would go through a $PM_{2.5}$ cyclone (URG-2000-30ED, USA) to
143 remove coarse particles, then was dried by a Nafion drier. The sampling line was assembled using
144 3/8" stainless steel tubes coated with the sponge to prevent water condensation.

145 The working principle of ToF-ACSM had been described in detail in previous studies (Ng et
146 al., 2011; Fröhlich et al., 2013). Briefly, a 100 μ m critical orifice and an aerodynamic lens were
147 settled in the front inlet system to focus the ambient particles into a concentrated and narrow beam
148 with a flow rate of ~84 cc/min. It should be mentioned that a $PM_{2.5}$ lens was used during the whole
149 campaign, which made the $PM_{2.5}$ measurement available (Xu et al., 2017).

150 The particle beam was transmitted through a vacuum chamber in which the gas-phase species
151 were separated from the particle beam. At the end of the vacuum chamber, the particles were
152 thermally vaporised at ~600 °C by impacting on a resistively heated porous tungsten surface. There
153 the non-refractory constituents in the particles flash vaporise and are subsequently ionised by a 70
154 eV electron impact. Finally, the ions were extracted by a set of ion optics and detected by the time-
155 of-flight mass spectrometer.

156 The ToF-ACSM was operated with a time resolution of 10 mins and scanned from m/z 10 to
157 219. The ionisation efficiency (IE) calibration was performed before and after the campaign
158 according to the proposal of a previous study (Fröhlich et al., 2013). Briefly, the size-selected (350
159 nm) NH₄NO₃ particles, which were generated by an aerosol generator, were simultaneously sampled
160 by the ToF-ACSM and a condensation particle counter (CPC 3775, TSI). Then, the IE can be
161 determined by comparing the response of ToF-ACSM to the mass of ammonium nitrate. The relative



162 ionisation efficiencies (RIEs) of sulphate and ammonium were also determined by sampling
163 $(\text{NH}_4)_2\text{SO}_4$ particles.

164 **2.3 Data process**

165 **2.3.1 ToF-ACSM data analysis**

166 The ToF-ACSM data analysis software (Tofware v2.5.13) written in Igor (Wavemetrics, Lake
167 Oswego, OR, USA) was used to analyse the mass concentration and chemical composition. The IE
168 value was 239 ions/pg, and the RIEs for sulphate and ammonium were 1.05 and 3.6, respectively.
169 For organics, nitrate and chloride, commonly used RIE values, i.e. 1.4, 1.1 and 1.3, were applied.
170 The algorithm proposed by (Middlebrook et al., 2012) to determine the collection efficiency (CE)
171 of ToF-ACSM was applied to quantify the aerosol species, as the acidity, chemical composition,
172 and phase state changed the particle bounce effects at the vaporiser (Matthew et al., 2008).

173 **2.3.2 PMF analysis**

174 The mass spectrum data matrix of OA was analysed by the PMF Evaluation Tool (PET, v2.08D)
175 (Paatero and Tapper, 1994; Ulbrich et al., 2009) in order to resolve distinct OA factors that might
176 be representative of specific sources. The PMF-ACSM data processing was followed by the
177 procedures proposed previously (Ulbrich et al., 2009; Zhang et al., 2011). Due to the weak signal
178 intensities, the ions with m/z over 120 were not included in the analysis. Any ions with signal-to-
179 noise (S/N) < 0.2 were removed from the analysis, and the ions whose S/N was 0.2–2 were down-
180 weighted by increasing their errors calculations by a factor of 2 (Sun et al., 2011). Different PMF
181 solutions were resolved by varying the factor number from 2 to 7. The solutions were evaluated by
182 comparing the mass spectral profiles of the output secondary aerosol factors as a function of the
183 rotational parameter (f_{peak}). Finally, a three-factor solution with $f_{\text{peak}} = 0$ was selected as our best
184 solution. The comparison of the results for three to five-factor solutions was described in detail in
185 Fig. S3 and Table. S2.



186 2.3.3 Identification of haze episodes

187 The haze episodes were defined by the daily $PM_{2.5}$ mass concentration exceeding Grade II
188 National Ambient Air Quality Standard (AAQS) of $75 \mu\text{g}/\text{m}^3$ for two successive days (Wang et al.,
189 2014). In the present study, we made some slight modifications to this definition following the
190 procedure of Zheng et al. (2016). Briefly, the periods during which the 24 h-moving average
191 concentration of $PM_{2.5}$ exceeds $75 \mu\text{g}/\text{m}^3$ for two successive days are regarded as episode candidates.
192 If the hourly $PM_{2.5}$ concentration during the first hour of an episode candidate is $50\text{--}75 \mu\text{g}/\text{m}^3$, then
193 the episode has a shape of 'slow start'; if it is $0\text{--}50 \mu\text{g}/\text{m}^3$, then the episode has the shape of the 'rapid
194 start'. Similarly, the shape at the end of an episode candidate can also be identified. Haze episodes
195 having a 'slow start' typically arise from the gradual accumulation of pollutants emitted both locally
196 and regionally under unfavourable meteorological conditions, while haze episodes having a 'rapid
197 start' are most likely related to regional transport (Zheng et al., 2015). Haze episodes having a 'slow
198 end' usually resulted from the gradual scavenge of pollutants.

199 According to the definition mentioned above, three haze episodes (denoted as H1, H2 and H3,
200 respectively, in Fig. 2), all with the types of 'slow start' and 'slow end', were identified over the whole
201 campaign. In addition, a fog event occurred during each haze episode (denoted as F1, F2 and F3,
202 respectively). Lacking the information of visibility and aerosol size distribution up to several tens
203 of micrometres, we were not able to precisely diagnose the accumulation and dissipation stages of
204 a fog event. Instead, we selected the hours with RH near 100 % as the duration of a fog event, which
205 was the same as the condition described in previous studies (Izhar et al., 2020; Guo et al., 2015).

206 2.4 Air mass trajectories analysis

207 2-day back trajectories arriving at the receptor site were calculated every hour over the whole
208 campaign using the National Oceanic and Atmospheric Administration (NOAA) HYSPLIT version
209 4 (Draxler and Hess, 1998). Input to the model is in the form of 1° latitude-longitude gridded
210 meteorological parameters from the Global Data Assimilation System meteorological dataset. We
211 chose an arrival height of 500 m which is above ground level (AGL) for target analysis in the
212 HYSPLIT model to diminish the effects of surface friction (Polissar et al., 2001); this height value
213 and greater are regarded as in the open height of the planetary boundary layer in winter and are more



214 useful for long-range transport. Finally, 839 backward trajectories in total were obtained. Then,
215 these trajectories were grouped into four clusters, i.e., Cluster1 from the north, Cluster2 from the
216 southwest, Cluster3 from the northeast, and Cluster4 from the east. The trajectories of each cluster
217 accounted for 12.6, 6.2, 58.4, and 22.8 % of total air mass trajectories during the whole campaign,
218 respectively.

219 **3. Results and discuss**

220 **3.1 Meteorological condition and chemical composition of NR-PM_{2.5}**

221 **3.1.1 Overview of meteorology and PM_{2.5} chemical composition**

222 The temporal variation of meteorological parameters, concentrations of gaseous pollutants, and
223 chemical compositions of PM_{2.5} over the whole campaign are illustrated in Fig. 2. The missing data
224 were due to the acquisition software malfunction of the instrument. During the campaign, the
225 temperature ranged from -1.9 to 16.3 °C with a mean value of 7.3 ± 2.8 °C, and the RH ranged from
226 35 to 100 % with an average of $81 \pm 12.4\%$. The wind from the southwest prevailed with an average
227 speed of 0.7 ± 0.5 m/s during the entire campaign. This indicated that the atmosphere was in a
228 stagnant state with relatively low temperature and high RH.

229 The mass concentration of NR-PM_{2.5} during the campaign ranged from 23 to 230 $\mu\text{g}/\text{m}^3$, with
230 an average of 98.5 ± 38.7 $\mu\text{g}/\text{m}^3$. This was comparable to the average PM_{2.5} concentrations during
231 wintertime in other cities in the SCB (Table S1). The OA concentration varied from several to 103
232 $\mu\text{g}/\text{m}^3$, with an average of 39.2 ± 3.9 $\mu\text{g}/\text{m}^3$, constituting the majority of PM_{2.5}. OA contributed ~20-
233 69 % to PM_{2.5} with an average of 40.3 ± 7.6 %. The average concentrations of nitrate, sulphate,
234 ammonium and chloride were 29 ± 14 (ranging from ~4 to 80 $\mu\text{g}/\text{m}^3$), 10 ± 4.2 (ranging from ~2 to
235 28 $\mu\text{g}/\text{m}^3$), 15.1 ± 6.4 (ranging from ~3 to 38 $\mu\text{g}/\text{m}^3$) and 5.2 ± 4.1 $\mu\text{g}/\text{m}^3$ (ranging from ~1 to 50
236 $\mu\text{g}/\text{m}^3$), taking up 28.8 ± 5.5 , 10.6 ± 2.8 , 15.3 ± 2.2 and 5.1 ± 3.1 % of PM_{2.5}, respectively. The
237 dominance of organic species was similar to previous observations in urban Chengdu during the
238 winter of 2014 and 2015 (Kong et al., 2020; Wang et al., 2018). However, the nitrate concentration
239 was higher than that of sulphate, which was contrary to that reported previously. A recent
240 observation in urban Chengdu also found that higher fraction of nitrate in PM_{2.5} compared to



241 sulphate, probably due to the remarkable decrease in SO₂ emission in the past ten years (Huang et
242 al., 2021; Fu et al., 2017).

243 3.1.2 Diurnal variation

244 The diurnal cycles of SO₂, NO₂, O₃, and PM_{2.5} compositions over the entire campaign were
245 depicted in Fig. 3. The concentration of NO₂ showed a bimodal distribution with peaks at 12:00 and
246 19:00, most likely due to the emission of vehicles. SO₂ concentration had a peak at 12:00, while the
247 peak concentration of O₃ was at 16:00.

248 Corresponding to the daily temporal variation of NO₂, nitrate, and ammonium showed similar
249 diurnal cycles with two peak concentrations, which indicated the simultaneous formation of these
250 two species. One of the peaks with a higher concentration showed at 13:00, and the other with a
251 lower concentration was at 20:00. The formation of nitrate and ammonium could be attributed to
252 photochemical processing during daytime and heterogeneous reactions during nighttime. Sulphate
253 showed a peak at 12:00, corresponding to the hour of daily maximum SO₂ concentration. The solar
254 radiation was also near the peak value at this time, suggesting the contribution of intense
255 photochemistry to sulphate formation (Weber et al., 2016).

256 Organics and chloride appeared to have similar diurnal cycles. The concentrations of these two
257 species increased gradually from 6:00 to 10:00 and then decreased till 16:00, which might be
258 affected by the change of planet boundary (PBL) height. After that, organics increased dramatically,
259 while chloride increased gradually and reached the second peak at 19:00. The time of these two
260 peaks were in accordance with rush hours, indicating the possible contribution of traffic emissions
261 to organics. Chloride was generally regarded as one of the tracers for biomass burning (Chantara et
262 al., 2019; Vicente et al., 2013). The peaks of chloride in the morning and evening were probably
263 due to the emission of biomass burning, which would also contribute to the increase of organics.

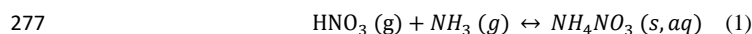
264 3.2 Characteristics of inorganic aerosol

265 The correlation between the molar equivalent concentrations of measured ammonium and the
266 sum of molar equivalent concentrations of nitrate, sulphate and chloride was illustrated in Fig. 4.
267 The slope of the regression line for ammonium against the sum of nitrate, sulphate and chloride with

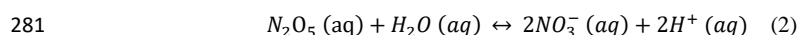


268 a value of 1.01 indicated that the anions in PM_{2.5} were well neutralised by cation (ammonium). This
269 result illustrated that nitrate, sulphate, and chloride were mainly in the form of NH₄NO₃, (NH₄)₂SO₄
270 and NH₄Cl, which were commonly considered secondarily formed (Ianniello et al., 2011; Ge et al.,
271 2017).

272 As SO₄²⁻ competed with NO₃⁻ for NH₄⁺ during their formation, the relationship between nitrate-
273 to-sulphate molar ratio ([NO₃⁻]/[SO₄²⁻]) and ammonium-to-sulphate molar ratio ([NH₄⁺]/[SO₄²⁻])
274 was indicative of the pathway of nitrate formation (He et al., 2012). If [NO₃⁻]/[SO₄²⁻] linearly
275 correlated with [NO₃⁻]/[SO₄²⁻] under ammonium-rich conditions ([NO₃⁻]/[SO₄²⁻] ≥ 1.5), the
276 homogeneous formation of nitrate was expected:



278 While for ammonium-poor conditions ([NO₃⁻]/[SO₄²⁻] < 1.5), the high concentration of nitrate
279 was attributed to its formation through hydrolysis of N₂O₅ on the pre-existing aerosols (Pathak et
280 al., 2009):



282 To better elucidate the factors affecting nitrate formation, we divided the observation period
283 into daytime (6:00 - 18:00, local time) and nighttime (18:00 - 6:00 next day, local time) hours. Fig.
284 S1 showed that the [NO₃⁻]/[SO₄²⁻] during both daytime and nighttime were larger than 1.5,
285 indicating ammonium-rich conditions. [NO₃⁻]/[SO₄²⁻] was significantly correlated with
286 [NH₄⁺]/[SO₄²⁻] during daytime with the regression function:

$$287 \quad \frac{\text{NO}_3^-}{\text{SO}_4^{2-}} = 0.69 \times \frac{\text{NH}_4^+}{\text{SO}_4^{2-}} - 1.08 \quad (3)$$

288 The intercept of the regression line on the [NH₄⁺]/[SO₄²⁻] axis was 1.56, which was close to
289 1.5 characterised by (Pathak et al., 2009), suggesting the nitrate formation was mainly driven by
290 HNO₃ production through the reaction of NO₂ + OH + M → HONO₂ + M. The formation of HNO₃
291 allowed the reaction between HNO₃ (g) and excess NH₃ (g) to happen, and thus generating
292 ammonium nitrate (Sun et al., 2011). Indeed, the nitrate concentration and nitrogen oxidation ratio
293 (NOR = n(NO₃⁻)/[n(NO₂) + n(NO₃⁻)]) increased as the Ox concentration increased (as shown in Fig.
294 5), and exhibited a strong O₃/Ox ratio dependency, which further demonstrated the homogeneous
295 formation of nitrate during daytime.

296 During nighttime, the O₃ concentration was low and ambient RH was relatively high, which



297 favoured the aqueous-phase reactions to occur. Higher nitrate concentration was observed with
298 increasing ALWC (as illustrated in Fig. S2(c)), and so was NOR. This phenomenon further
299 demonstrated that nitrate was mainly formed through aqueous-phase reactions during nighttime.
300 The regression function between $[\text{NO}_3^-]/[\text{SO}_4^{2-}]$ and $[\text{NH}_4^+]/[\text{SO}_4^{2-}]$ was expressed as:

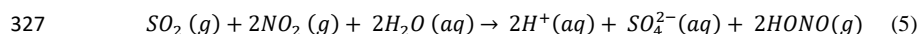
$$301 \quad \frac{[\text{NO}_3^-]}{[\text{SO}_4^{2-}]} = 0.69 \times \frac{[\text{NH}_4^+]}{[\text{SO}_4^{2-}]} - 1.24 \quad (4)$$

302 The intercept of the regression line on the $[\text{NH}_4^+]/[\text{SO}_4^{2-}]$ axis was 1.80, larger than 1.5. The
303 regression function suggested that nitrate formation was mainly attributed to homogeneous reactions,
304 which was not in accordance with the domination of aqueous-phase reactions for nitrate formation
305 during nighttime as discussed above. It seemed that the intercept of 1.5 for the regression line on
306 the $[\text{NH}_4^+]/[\text{SO}_4^{2-}]$ axis might not be an appropriate proxy to define the formation process of
307 nocturnal nitrate in the present study, because the emission of NO_x and SO_2 had been reduced while
308 NH_3 increased in the past almost ten years, which resulted in the ammonium-rich condition in the
309 atmosphere (Fu et al., 2017; Liu et al., 2018). The abundant NH_3 in the atmosphere could
310 accommodate plenty of basic species during the heterogeneous formation of nitrate, which was
311 usually considered to occur under ammonium-lean conditions though (Pathak et al., 2009). We
312 deduced that HNO_3 was firstly heterogeneously formed through the hydrolysis of N_2O_5 , then excess
313 NH_3 was uptake by wet particles and neutralised HNO_3 forming ammonium nitrate (Man et al.,
314 2015; Wen et al., 2018). The results were consistent with the study of (Tian et al., 2019), which
315 demonstrated that heterogeneous hydrolysis of N_2O_5 dominated nitrate formation during nighttime,
316 while photochemical reactions played an important role in nitrate formation during daytime.

317 Fig. S2(b) showed that the average sulphate concentration increased when $\text{Ox} > 60 \mu\text{g}/\text{m}^3$,
318 which corresponded to daytime hours, suggesting the contribution of the photochemical process to
319 sulphate formation. However, the sulphur oxidation ratio ($\text{SOR} = n(\text{SO}_4^{2-})/[\text{n}(\text{SO}_2) + \text{n}(\text{SO}_4^{2-})]$)
320 decreased with increasing Ox , suggesting the photooxidation was not efficient for converting SO_2
321 to sulphate. By contrast, SOR showed an increasing trend as ALWC increased, demonstrating the
322 efficient conversion of SO_2 to sulphate through aqueous-phase reactions. A previous study showed
323 that the aqueous oxidation of SO_2 by NO_2 is key to efficient sulphate formation on fine aerosols
324 with high relative humidity and NH_3 neutralisation (Wang et al., 2016). As mentioned above, the
325 atmospheric aerosols were well neutralised, and RH was high, which favoured the following



326 reaction to occur:



328 **3.3 Characteristics of organic aerosol**

329 **3.3.1 Source appointment of OA**

330 PMF analysis was performed to explore the OA sources measured during the whole campaign.
331 A three-factor solution was chosen as the best PMF analysis results based on the mass spectra profile,
332 variation of Q/Q_{exp}, diurnal variation and correlation with external tracers. The resolved factors
333 included a hydrocarbon-like OA (HOA), a biomass burning OA (BBOA) and an oxygenated OA
334 (OOA). The mass spectra profiles of these three factors were shown in Fig. 6, and the temporal
335 profile of each factor and its external tracer were also shown.

336 The mass spectrum of HOA was dominated by the ions of m/z 29, 41, 55, 57, 69 and 71. HOA
337 was well correlated with BC ($r = 0.77$), which was largely emitted by vehicles. The diurnal cycles
338 of HOA showed two peaks during typical rush hours, demonstrating the contribution of traffic
339 emissions to HOA (Lanz et al., 2007; Zhang et al., 2005). The average concentration of HOA was
340 $8.9 \pm 6.5 \mu\text{g}/\text{m}^3$ and constituted $24.2 \pm 10.4 \%$ of OA over the whole campaign. The increased
341 fraction of HOA as a function of total OA (Fig. 7) demonstrated the contribution of motor vehicle
342 emissions to haze formation.

343 BBOA was characterised by the pronounced peaks at m/z 60 (mainly $\text{C}_2\text{H}_4\text{O}_2^+$) and 73
344 ($\text{C}_3\text{H}_5\text{O}_2^+$), which were generally regarded as biomass burning markers from levoglucosan
345 compounds (Mohr et al., 2012; Weimer et al., 2008; Alfara et al., 2007). BBOA was well correlated
346 with m/z 60 and m/z 73 ($r = 0.76$ and 0.94 , respectively) and accounted for 88 % of m/z 60 and 70 %
347 for m/z 73, which were higher than those in other sources. A good correlation was also found
348 between BBOA and chloride ($r = 0.64$), which was also suggested to be one of the tracers of biomass
349 burning. The diurnal variation of BBOA showed a similar trend of chloride, with two peaks during
350 8:00-10:00 and at 19:00, which was due to the residential cooking and heating using biomass. The
351 concentration of BBOA ranged from ~ 1 to $34 \mu\text{g}/\text{m}^3$, with an average of $8.9 \pm 5.4 \mu\text{g}/\text{m}^3$. BBOA
352 took up $24.2 \pm 8.6 \%$ with a maximum of 46 % of OA, and its fraction also increased with increasing



353 total OA concentration, indicating the contributions of biomass burning activities during haze
354 episodes.

355 OOA was featured by the dominant signal intensities at m/z 28 (mainly CO^+) and m/z 44 (CO_2^+).
356 OOA accounted for 69 % of m/z 44, which was higher than those in other sources. The time series
357 of OOA correlated well with those of nitrate and sulphate ($r = 0.81$ and 0.72 , respectively),
358 suggesting the commonly regional and aged properties of OOA. The concentration of OOA
359 accumulated gradually from 8:00 to 13:00, then decreased till night time. The diurnal cycle of OOA
360 was similar to solar radiation, suggesting OOA formation was associated with photochemical
361 reactions. The average OOA concentration showed increasing trends as Ox concentration increased
362 during both daytime and nighttime (Fig. S4), indicating the probable formation pathways of OOA
363 from its precursors (Kuang et al., 2020; Zhan et al., 2021). Note that the accumulation of NO_2 would
364 lead to the decrease of O_3/Ox ratio at night; thus, Ox might not be an appropriate indicator of
365 photochemical oxidation (Xu et al., 2017; Herndon et al., 2008). The OOA formation might be
366 attributed to other processes during nighttime. For example, previous studies showed that high NO_x
367 concentration facilitated the formation of nitrate radical (NO_3), and the NO_3 oxidation of biogenic
368 volatile organic compounds (BVOC) was important for nighttime secondary organic aerosol
369 formation (Boyd et al., 2017; Rollins et al., 2012). The average OOA concentration did not change
370 significantly with increasing ALWC during daytime, suggesting the less contribution of aqueous-
371 state reaction to the formation of OOA. During nighttime, the average OOA concentration showed
372 an increasing trend when $\text{ALWC} < 200 \mu\text{g}/\text{m}^3$ and kept relatively constant subsequently, suggesting
373 the aqueous-phase reactions did not significantly affect the formation of OOA.

374 3.3.2 Elemental composition of OA

375 The f_{44} vs. f_{43} and f_{44} vs. f_{60} during the entire campaign were illustrated in Fig. 8. The triangle
376 plot of f_{44} vs. f_{43} has been widely used to characterise OA evolution in the atmosphere because
377 m/z 's 44 and 43 are usually from different functional groups, and the ratio changes as a function of
378 atmospheric aging. The f_{43} ranged from ~ 0.06 to 0.12 with an average of 0.08 ± 0.009 , and the
379 range of f_{44} was ~ 0.07 - 0.24 with an average of 0.15 ± 0.03 , suggesting the existence of both fresh
380 and aged aerosols in the atmosphere. Most of the data were within the triangle space characterised



381 by a series of field observations and experimental data (Ng et al., 2011). However, those points with
382 higher f_{44} were outside the upper boundary of the triangle region, suggesting the corresponding
383 aerosols were more oxidised. It could be observed that the points with higher f_{44} (> 0.16)
384 corresponded to relatively higher Ox concentration and lower RH, while those with lower f_{44}
385 corresponded to relatively lower Ox concentration and higher RH, suggesting that the formation of
386 more oxidised OOA was mainly attributed to photochemical reactions, and the formation of less
387 oxidised OOA was probably attributed to aqueous-state reactions (Zhao et al., 2019; Kim et al.,
388 2019).

389 The triangle plot of f_{44} vs. f_{60} was widely used as a metric to access the evolution of
390 atmospheric BBOA (Cubison et al., 2011). A value of 0.003 for f_{60} was recommended as an
391 appropriate value to represent the atmospheric background free of biomass burning influence (Aiken
392 et al., 2009; Docherty et al., 2008). The f_{60} ranged from 0.0028 to 0.055 with an average of 0.008
393 ± 0.003 during the campaign. Except for several points, the f_{60} was ubiquitously higher than 0.003
394 and most points fell in the triangular region, suggesting the contribution of biomass burning to OA.
395 The f_{44} and f_{60} of BBOA resolved by PMF in the present study were also in the triangular region
396 and comparable with previous studies (Paglione et al., 2020; Zhao et al., 2019; Kim et al., 2019).
397 Fig. S5 showed that f_{44} increased while f_{60} decreased with increasing Ox, indicating the likely
398 oxidation of levoglucosan and/or levoglucosan-like substances. Cubison et al. (2011) suggested that
399 the increasing f_{44} was not only attributed to the oxidation of levoglucosan-like species, but the
400 oxidation of bulk OA also played a role because the levoglucosan-like species only contributed a
401 small fraction of the OA mass (Aiken et al., 2009). Their contribution to the total signal m/z 44
402 before or after aging was also small. Compared to the effects of Ox, the increasing RH did not seem
403 to push f_{60} to the left upper region. Higher RH was observed for those data points within the region
404 of aged BBOA in the f_{44} vs. f_{60} space, as reported previously by Paglione et al. (2020), which
405 indicated the probable aqueous-phase oxidation of BBOA. Although the aqueous OOA (aq-OOA)
406 could not be resolved in the present study, we deduced that the aqueous-phase reactions occurred
407 and contributed to the formation of OOA, for (1) the ambient RH was typically above 65%, which
408 favoured the presence of wet aerosol particles; (2) the range of O/C estimated from the Improved-
409 Ambient (IA) method varied from 0.46 to 0.85 when the ambient RH $> 80\%$, covering the O/C
410 range of the OOA obtained from the photooxidation of organic precursors in the aqueous phase and



411 ambient aq-OOA observed in many other cities (Duan et al., 2021; Mandariya et al., 2019; Sun et
412 al., 2010; Xu et al., 2017; Gilardoni et al., 2016).

413 The evolution of OA during the whole campaign was characterised by the van Krevelen (VK)
414 diagram in Fig. 9. The slope obtained from the linear regression of H:C versus O:C plotted in the
415 $\text{VK-}\overline{\text{OS}}_c$ space could be used to infer the composition of OA and the chemical process in OA
416 formation (Docherty et al., 2018). The slope of 0 in $\text{VK-}\overline{\text{OS}}_c$ plot was related to the replacement of
417 a hydrogen atom with an OH moiety, while the slopes of -0.5 and -1 indicated the formation of
418 carboxylic groups with/without fragmentation, and a slope of -2 was equivalent to the replacement
419 of an aliphatic carbon with a carbonyl group (Heald et al., 2010; Ng et al., 2011). The slope of the
420 linear fitting line for all the data points was -0.14, suggesting the probable formation of carboxylic
421 acid moieties and hydroxyl groups. The slopes of the linear fitting lines for each fog episode were similar
422 and close to zero, which was consistent with the hydroxyl group formation possibly taking place in
423 aerosol water through dark chemistry (Sun et al., 2010; Yu et al., 2014; Zhao et al., 2014).

424 **3.4 Case studies for haze pollution**

425 **3.4.1 Factors driving the evolution of haze episodes**

426 As mentioned above, three haze episodes were identified over the whole campaign. The
427 synoptic conditions and aerosol chemical composition for each haze episode were summarised in
428 Table. S2. The average temperature during H2 was lower than those during H1 and H3, while the
429 average SR was higher. The mean RH and wind speed were almost the same during each haze
430 episode. The average concentrations of aerosol chemical composition and their contributions to
431 $\text{PM}_{2.5}$ were different in each haze episode, indicating that the factors causing haze formation might
432 be different during the campaign.

433 The average $\text{PM}_{2.5}$ concentrations measured by ToF-ACSM during H1, H2, and H3 were 113
434 ± 46 , 109 ± 46 , and $104 \pm 30 \mu\text{g}/\text{m}^3$, respectively. The average mass fractions of OA, nitrate, sulphate,
435 ammonium, and chloride were similar during H1 and H3 (as shown in Fig. 10(a)). During H2, the
436 mass fractions of sulphate and ammonium were slightly higher than those in H1 and H3, while the
437 mass fractions of OA and chloride were lower. In OA, the fraction of primary organic aerosols (POA
438 = HOA + BBOA) during H3 was higher than those during H1 and H2. The fraction of BBOA showed



439 an increasing trend from H1 to H3, demonstrating the contribution of biomass burning to haze
440 formation. Despite the importance of BBOA to winter haze formation in SCB, the control of biomass
441 burning did not receive much attention, and more efforts were needed for atmospheric aerosol
442 mitigation in the future.

443 Fig. 10(b) showed that the concentrations of OA, nitrate, sulphate, ammonium, and chloride
444 all increased as the ambient air quality worsened (implying by the increasing $PM_{2.5}$ concentration)
445 during each haze episode. During H1, the fraction of nitrate in $PM_{2.5}$ increased, while the proportions
446 of sulphate, OOA, and HOA in $PM_{2.5}$ decreased as the $PM_{2.5}$ concentration increased, indicating the
447 evolution of this haze episode was mainly driven by the reactions involving nitrate formation. For
448 H2, the fraction of nitrate and ammonium in $PM_{2.5}$ did not show apparent changes, and the fractions
449 of sulphate and OOA decreased, while the fractions of BBOA and HOA increased as the air quality
450 worsened, demonstrating that the emission of primary organic aerosols from biomass burning and
451 vehicle exhaust were the major factors which drove the haze formation. During H3, the fractions of
452 nitrate and BBOA in $PM_{2.5}$ increased, while OOA decreased and the rest composition did not change
453 significantly as the $PM_{2.5}$ concentration increased, showing that the evolution of this haze episode
454 was mainly driven by the reactions involving nitrate formation and biomass burning.

455 The average estimated O:C and H:C during H1 and H2 were similar and slightly higher/lower
456 than that during H3, thus resulting in a higher carbon oxidation state ($\overline{OS}_c \approx 2O:C - H:C$) during
457 H1 and H2. The lower average \overline{OS}_c during H3 might be due to the higher proportion of HOA and
458 BBOA, which did not undergo long-time aging and kept relatively fresh in the atmosphere.

459 3.4.2 Regional transport

460 Air mass from the north (Cluster1) transported at relatively high heights before arriving at the
461 observation site (as illustrated in Fig. 11), and corresponded to the lowest average $PM_{2.5}$
462 concentration ($66 \pm 30 \mu\text{g}/\text{m}^3$). The air mass of Cluster2 had the longest transport distance and
463 highest transport height. Although they took up the least proportion of total air mass, they had the
464 highest average $PM_{2.5}$ concentration ($119 \pm 30 \mu\text{g}/\text{m}^3$) during the whole campaign, suggesting that
465 pollutants accumulated high in the air. Air parcels from the east (Cluster3) with the shortest transport
466 distance and relatively low transport height had an average $PM_{2.5}$ concentration of $113 \pm 34 \mu\text{g}/\text{m}^3$.



467 This indicated that the pollutants might be brought to the observation site along with the transport
468 of air mass originating from adjacent areas. The air mass from the northeast of Sichuan province
469 (Cluster4) had the lowest transport height; however, the corresponding $PM_{2.5}$ concentration was
470 lower than that of Cluster3.

471 Compared to cluster1 and cluster4, a higher contribution of nitrate to $PM_{2.5}$ was observed for
472 Cluster2 and Cluster3, which was mainly related to the intense emission from industry and vehicles.
473 However, the contribution of BBOA was higher for Cluster3 and Cluster4 compared to other clusters,
474 suggesting intense biomass burning along their transport paths.

475 To better understand the potential pollutant sources during the campaign, the potential source
476 contribution function (PSCF) was applied to analyse the possible regions that might contribute to
477 haze formation. The spatial distribution of weighted PSCF for different chemical compositions was
478 illustrated in Fig. 12. The WPSCF values for organics over the southwest and southeast were > 0.7 ,
479 indicating these locations were likely source areas of organics. For nitrate and sulphate, the areas
480 by the southwest and south of the sampling site were potential source regions. The major source
481 regions for HOA were the areas of south Sichuan province and southwest Deyang. The regions
482 contributing to BBOA were the areas of east Sichuan province, which was consistent with a higher
483 proportion of BBOA in $PM_{2.5}$ in the air mass stemming from these locations. For OOA, the WPSCF
484 values over the southwest and southeast of Deyang and northeast Sichuan province were > 0.7 ,
485 suggesting the contribution of these regions.

486 **3.5 Evolution of chemical composition during fog periods**

487 The fog periods usually started at night or early morning and dissipated in the afternoon. The
488 individual meteorological parameter differed among each fog period (as summarised in Table S3).
489 The average temperature was the highest during F1 (6.2 ± 2.3 °C), and the lowest was observed
490 during F2 (1.5 ± 3.2 °C). The maximum solar radiation during F1 and F2 (470 and 500 W/m^2) were
491 similar and much higher than that during F3 (75 W/m^2). The synoptic conditions with low
492 temperature and calm wind favoured the formation of radiation fogs in each fog period.

493 The chemical composition of $PM_{2.5}$ was also different during each fog period. The average
494 concentrations of organics, nitrate, and ammonium were almost the same during F2 and F3 and



495 significantly lower than those during F1. However, the average chloride concentration during F2
496 was twice of those during F1 and F3, suggesting the possibility of stronger biomass burning
497 emissions during F2. OOA constituted the major part of OA during F1, while HOA and BBOA were
498 more important than OOA during F2 and F3. The domination of secondary species in $PM_{2.5}$ during
499 F1 was probably due to the aqueous-phase reaction, while the primary emission tended to be
500 stronger during F2 and F3.

501 Since the aerosols were dried by a Nafion drier, the aerosols that ToF-ACSM measured were
502 the interstitial particles in droplets or those excluded from fog droplets. In order to better characterise
503 the evolution of chemical composition in each fog period, the intervals for 3 h before and after the
504 fog period, when ambient RH was lower than 95 %, were regarded as pre-fog and post-fog periods,
505 respectively (Kim et al., 2019). Note that the post-fog was not assigned for F3 because the ToF-
506 ACSM data were not available with a failure of acquisition software.

507 The average concentrations of different chemical compositions during the evolution of fog
508 episodes (pre-fog, during fog, and post-fog) were illustrated in Fig. 13. Compared to the pre-fog
509 period of F1, all species in the interstitial aerosols decreased during the foggy period, likely due to
510 the scavenging by fog droplets. Note that the OOA and sulphate decreased less than other species,
511 probably due to the OOA and sulphate formation through aqueous-phase reactions against the
512 scavenging effect of fog droplets. Except for OOA and nitrate, all species kept decreasing during
513 post-fog periods, which might be attributed to the increase of the PBL height. The increase of OOA
514 and nitrate was probably associated with the enhancement of photochemical reaction after the
515 dissipation of fog.

516 Distinguished from F1, all species (except for HOA) increased during the foggy period from
517 the pre-fog period during F2. Although hydrophilic species (e.g., nitrate, sulphate, and OOA) tended
518 to be scavenged by fog droplets, it seemed that the formation of OOA, nitrate, sulphate, and
519 ammonium was significantly faster than wet removal, thus resulting in an increase during the foggy
520 period. BBOA and HOA were commonly considered as hydrophobic species, and they were
521 excluded from fog droplets. Previous studies showed that BBOA and HOA concentrations decreased
522 during the foggy period compared to the pre-fog period (Collett et al., 2008; Kim et al., 2019),
523 despite their insoluble nature. The increase of BBOA in the present study was attributed to the
524 intense emission from biomass burning during the foggy period, which overwhelmed the scavenging



525 effects of fog droplets. During the post-fog period, BBOA and HOA decreased significantly,
526 possibly due to weaker emission and the efficient removal of fog droplets through nucleation and/or
527 coagulation. The dynamics of PBL might also play a role because the temperature kept increasing,
528 and higher PBL was expected during the post-fog period. With stronger solar radiation, OOA, nitrate,
529 and ammonium continued growing during the post-fog period from the foggy period through
530 photochemical reactions. However, sulphate slightly decreased, which might be due to the
531 insufficient formation through photochemical reactions, and decreased as the PBL height increased.
532 Similar to F2, all the secondary species increased during the foggy period from the pre-fog period
533 during F3. However, BBOA and HOA were reduced significantly by the scavenging of fog droplets.

534 The average elemental O:C showed an increasing trend from pre-fog periods to post-fog/foggy
535 periods, while H:C did not change significantly for different fog events, suggesting the OA became
536 more oxidised. As shown in Fig. S6, the mass fractions of OOA increased, while the contribution of
537 BBOA and HOA decreased from pre-fog periods to post-fog/foggy periods for the three fog events.
538 As a consequence, the O:C increased in line with the increased contribution of OOA. Previous
539 studies had reported that the aqueous-phase reactions enhanced OOA formation during fog/high RH
540 periods (Chakraborty et al., 2016; Kuang et al., 2020; Chakraborty et al., 2015). It appeared that the
541 OOA formation would balance out the scavenging of fog droplets during the foggy period for the
542 three fog events, despite the hydrophilic OOA being preferentially scavenged by fog droplets. Thus,
543 the OOA concentration marginally decreased or even increased during foggy periods.

544 4. Conclusions

545 Haze pollution has long been a severe environmental problem in SCB. The formation process
546 of haze pollution in SCB might be different from those in NCP, YRD, and PRD due to the unique
547 topography and meteorological conditions, which are still unclear. Based on the measurement data
548 of a ToF-ACSM and combined with the PMF and PSCF analysis, the temporal variation, formation
549 process, and sources of PM_{2.5} were characterised to elucidate further the factors contributing to haze
550 formation. It was found that the concentrations of OA and nitrate increased dramatically as PM_{2.5}
551 concentration increased, and the stagnant synoptic condition favoured the accumulation of these
552 pollutants. For different haze events, the driving factors could be classified into three types: one was



553 the reactions involving nitrate formation; another one was the intense biomass burning and vehicle
554 exhaust emissions, and the last one was the combination of the reactions involving nitrate formation
555 and biomass burning. Nitrate formation was primarily affected by photooxidation during daytime,
556 while the nocturnal nitrate formation was dominated by aqueous-phase reactions. OOA constituted
557 a major part of OA, and it was mainly generated through photooxidation, while aqueous-phase
558 reactions did not significantly promote its formation.

559 Due to the limitation of the present study, the parameters which are indicative of the pathways
560 of nitrate formation are not characterised. The major precursors contributing to a large amount of
561 OOA are not clear yet. In addition, how controlling BBOA will affect the atmospheric visibility,
562 radiative forcing, and climate change in SCB needs further investigation in the future. In spite of
563 the deficiencies, the results in this study implied that controlling primary emissions (such as biomass
564 burning and vehicle exhaust) and precursors of secondary aerosols (e.g., NO_x, SO₂, and VOCs)
565 during severe haze periods will benefit the improvement of air quality in SCB.

566
567



568 *Data availability.* The data generated and analysed in this study are available on visiting
569 <https://doi.org/10.5281/zenodo.6965551>.

570

571 *Author contributions.* FY and SX designed this study. XZ and QL contributed to data collection
572 during the field campaign. JZ, DZ, and CZ performed field experiments. ZL and CP performed the
573 data analysis. ZB wrote the manuscript. GS, LZ, and YC contributed to the scientific discussion and
574 paper correction.

575

576 *Competing interests.* The authors declare that they have no conflict of interest.

577

578 *Acknowledgements.* This work was supported by the National Key Research and Development Program of China
579 (grant no. 2018YFC0214001), and the National Natural Science Foundation of China (grant no. 42075109).

580

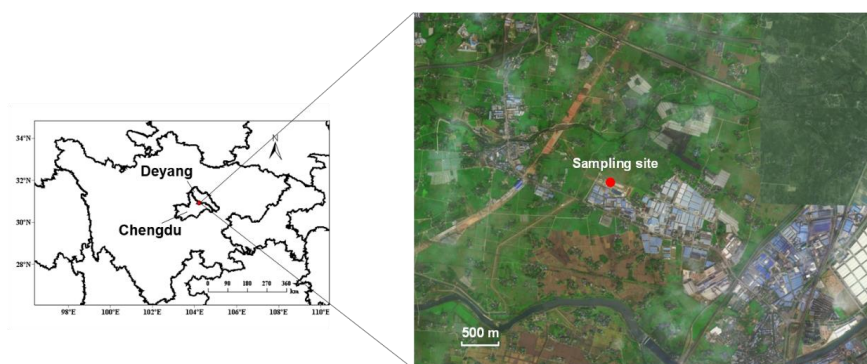
581 *Financial support.* This research has been supported by the National Key Research and Development Program of
582 China (grant no. 2018YFC0214001), and the National Natural Science Foundation of China (grant no. 42075109).

583

584



585



586

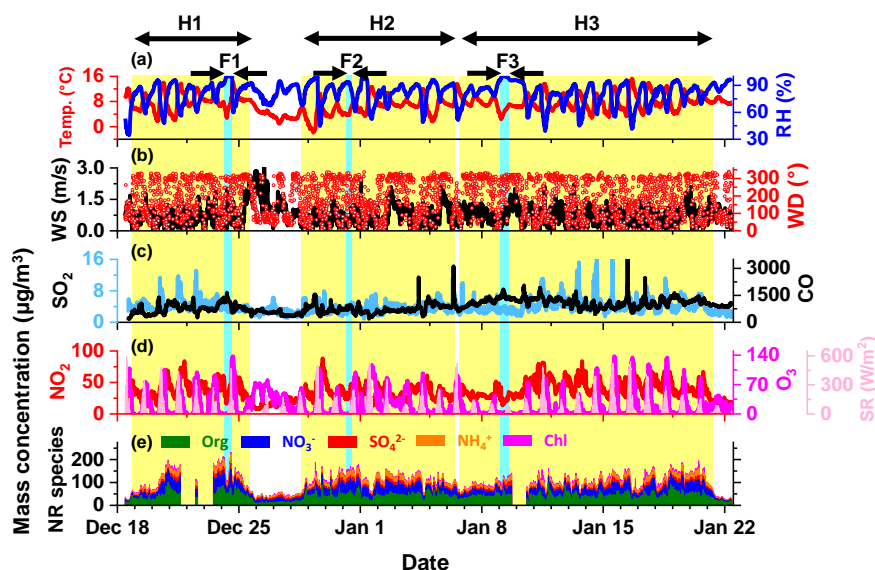
587

Fig. 1 Location of the observation site ([from Baidu Maps, ©2022 Baidu – GS\(2021\)6026](#)).

588



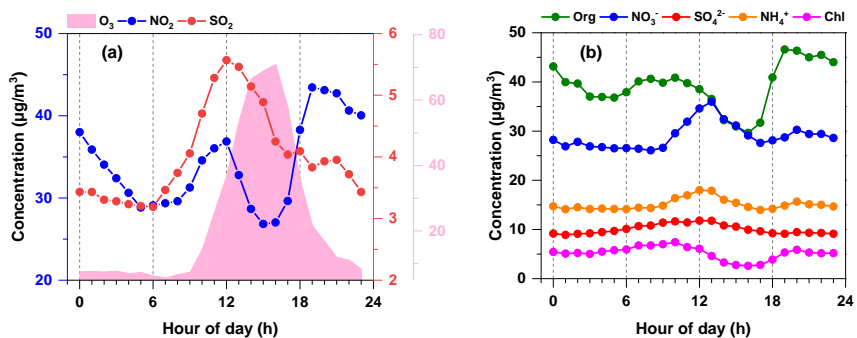
589



590

591 Fig. 2 Time series of (a) relative humidity (RH) and temperature (T); (b) wind direction and wind
592 speed; (c), (d) CO, NO₂, SO₂, and O₃ mass concentrations and solar radiation; (e) mass concentration
593 of organics, nitrate, sulphate, ammonium, and chloride in NR-PM_{2.5}. The yellow-shaded areas
594 represent the intervals of H1, H2, and H3, respectively. The light blue-shaded areas represent the
595 intervals of F1, F2, and F3, respectively.

596



597

598

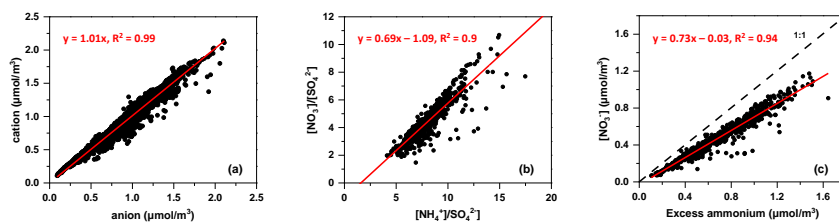
Fig. 3 Diurnal variations of (a) O_3 , NO_2 , and SO_2 , (b) chemical composition in NR- $\text{PM}_{2.5}$.

599

600



601



602

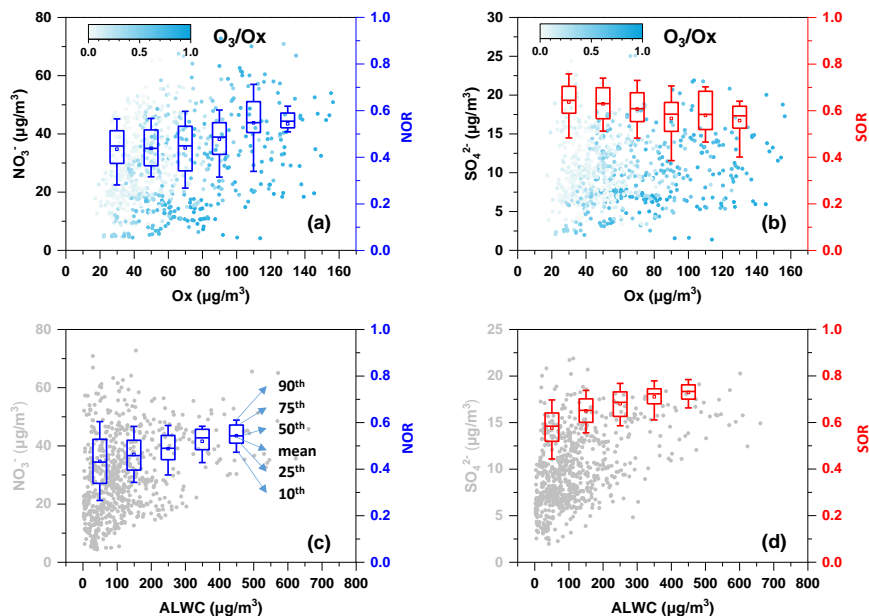
603 Fig. 4 Scatter plots of (a) molar concentrations of cations vs. anions, (b) molar ratios of nitrate to
604 sulphate vs. ammonium to sulphate, and (c) molar concentrations of nitrate vs. excess ammonium.

605

606



607



608

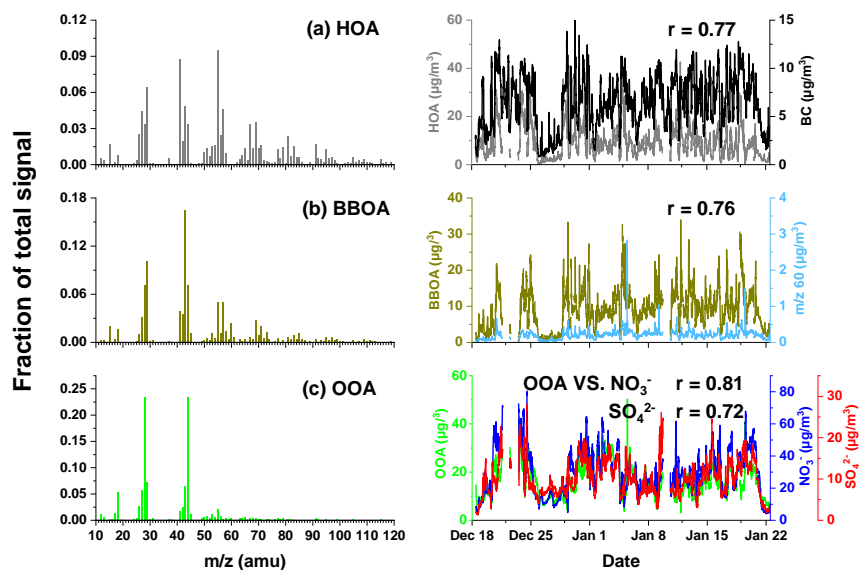
609 Fig. 5 Variation of (a), (c) nitrate and NOR and (b), (d) sulphate and SOR as Ox/ALWC increases.
610 The data NOR and SOR were grouped into different bins according to 20 $\mu\text{g}/\text{m}^3$ increment of Ox in
611 (a) and (b), and 100 $\mu\text{g}/\text{m}^3$ increment of ALWC in (c) and (d). The colour scale represents O_3/Ox
612 ratios in (a) and (b). The mean (square), 50th (horizontal line inside the box), 25th and 75th
613 percentiles (lower and upper box), and 10th and 90th percentiles (lower and upper whiskers) of the
614 box chart are marked in (c). The concentration of ALWC was simulated using the ISORROPIA-II model.

615

616



617



618

619 Fig. 6 Mass spectrum of (a) HOA, (b) BBOA, and (c) OOA resolved by PMF. The time series of

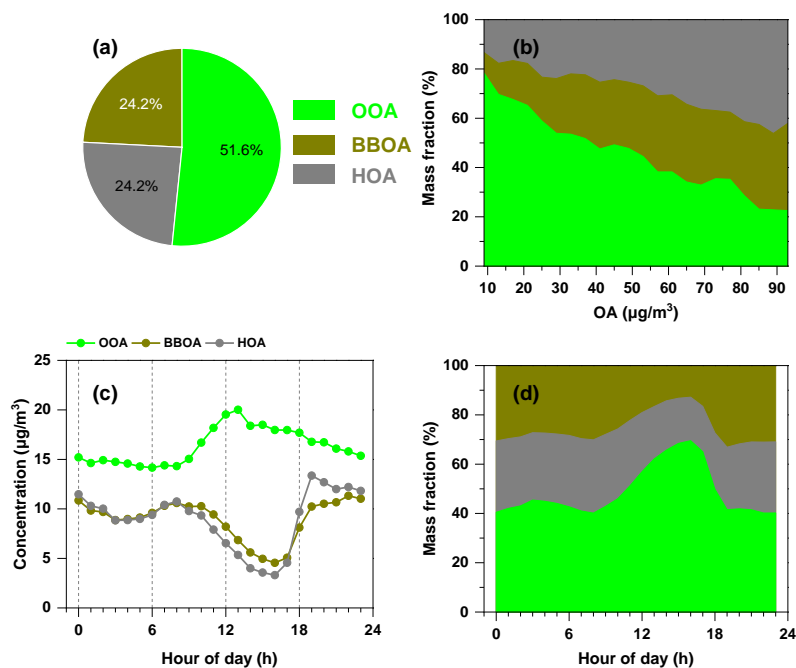
620 each OA source and corresponding tracers are depicted in the right panel.

621

622



623



624

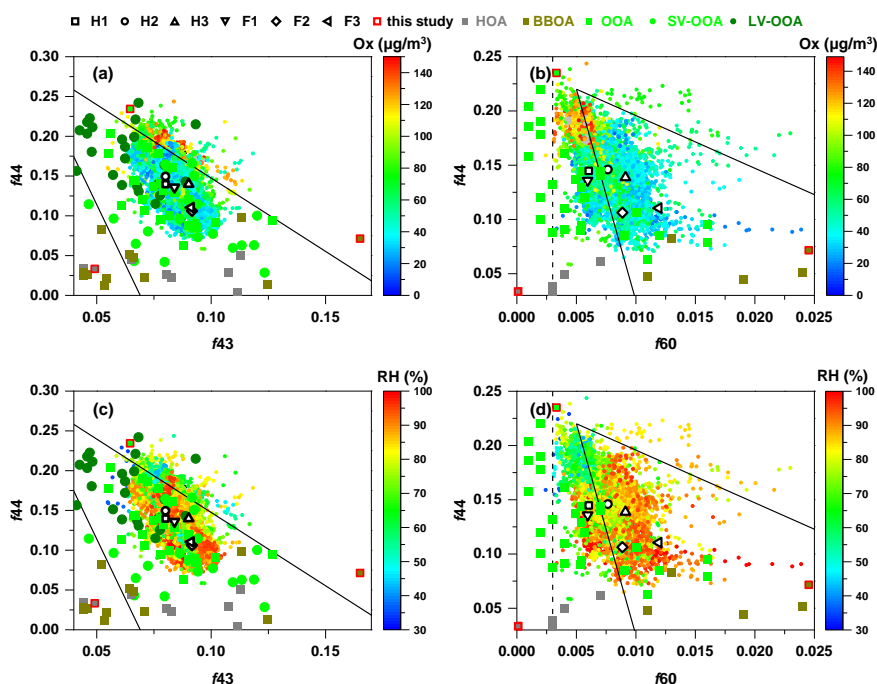
625 Fig. 7 Average mass fraction of different OOA, BBOA, and HOA (a) in OA and (b) as a function of
626 OA mass concentration. The diurnal variation of different OA compositions and their mass
627 contributions are shown in (c) and (d).

628

629



630



631

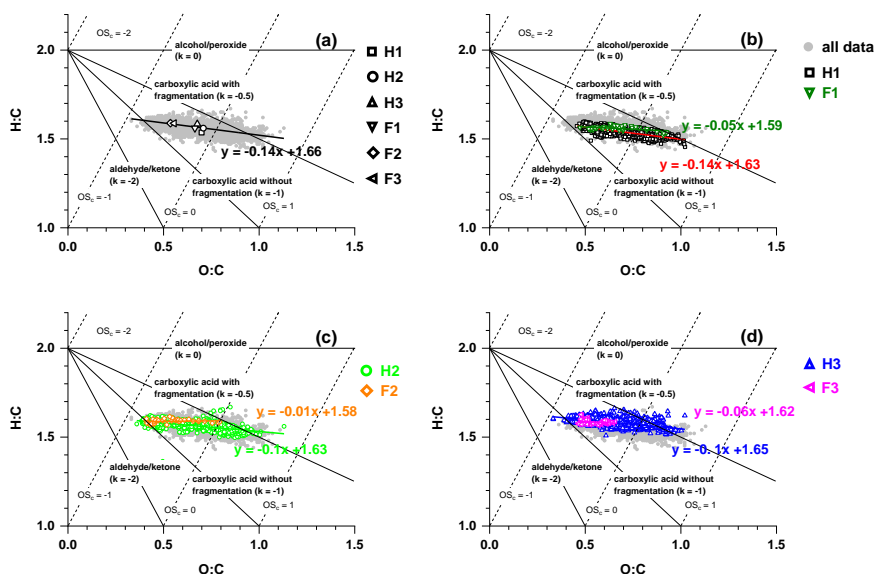
632 Fig. 8 Triangle plots of (a), (c) f_{44} (ratio of m/z 44 to total signal in the component mass spectrum)
633 vs. f_{43} (ratio of m/z 43 to total signal in the component mass spectrum), and (b), (d) f_{44} vs. f_{60}
634 (ratio of m/z 60 to total signal in the component mass spectrum) during the whole campaign. The
635 colour scale in (a) and (b) represents Ox concentration, and that in (c) and (d) represents RH. The
636 solid lines in (a) and (c) are derived from the results reported by Ng et al. (2010). The dashed line
637 representing the background value of secondary aged OA and the solid guidelines in (b) and (d) are
638 derived from Cubison et al. (2011). The f_{44} vs. f_{43} and f_{44} vs. f_{60} for different OA sources reported
639 in previous studies are also shown (Kim et al., 2019; Ng et al., 2011; Wang et al., 2016; Zhao et al.,
640 2019; Paglione et al., 2020).

641

642



643



644

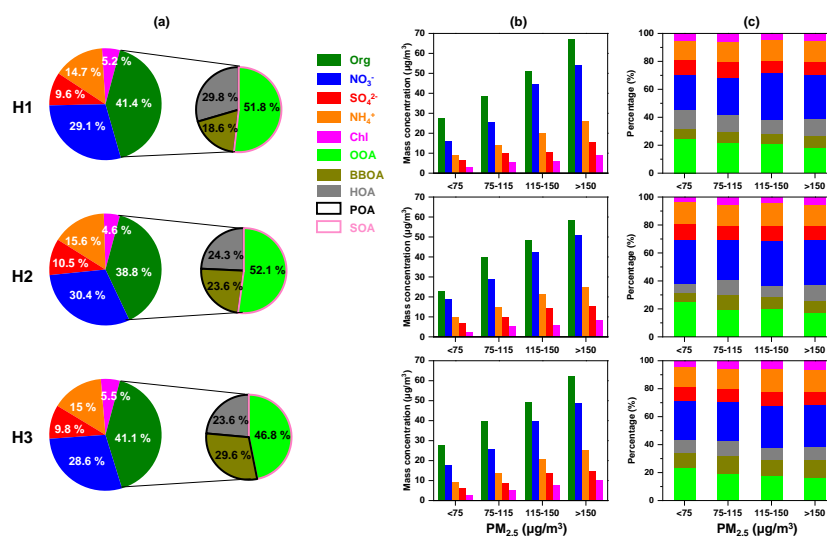
645 Fig. 9 The Van Krevelen- \overline{OS}_c diagram with data during (a) the whole campaign, (b) H1 and F1, (c)
 646 H2 and F2, and (d) H3 and F3. The triangle lines with different slopes show distinct formation
 647 processes (Heald et al., 2010).

648

649



650



651

652 Fig. 10 (a) Average mass fractions of different chemical compositions in PM_{2.5}, (b) mass

653 concentration, and (c) relative contribution of inorganic/organic species as a function of PM_{2.5}

654 concentration during each haze episode. The right panel in (a) depicts the contribution of OOA,

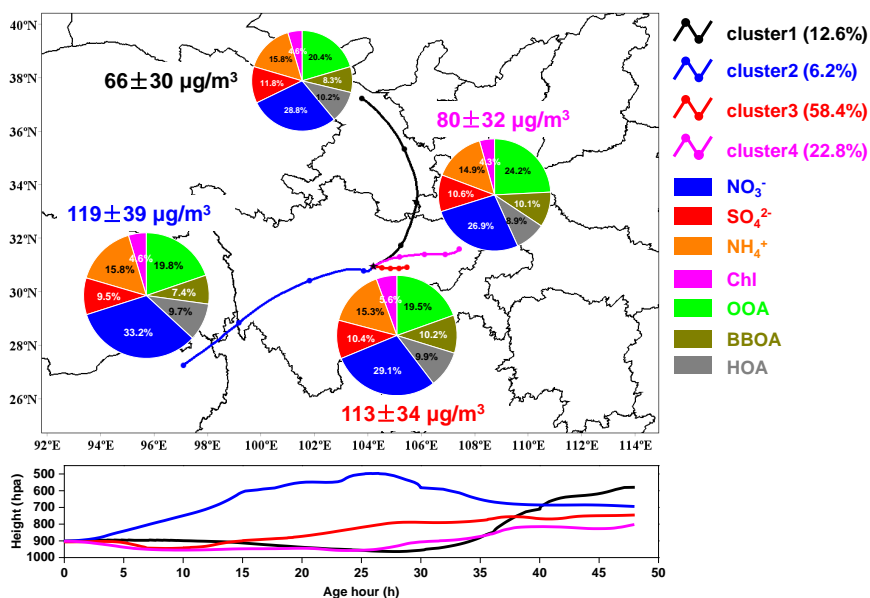
655 BBOA, and HOA to OA.

656

657



658



659

660 Fig. 11 Simulation results of 48 h backward air mass cluster-mean trajectories during the campaign.

661 The lines in black, blue, red, and purple represent the mean trajectories of Cluster1 to Cluster4,

662 respectively. The pie charts show the average mass contribution of different chemical compositions

663 to $PM_{2.5}$ for each cluster. The lower panel shows the height profile for different air mass clusters along

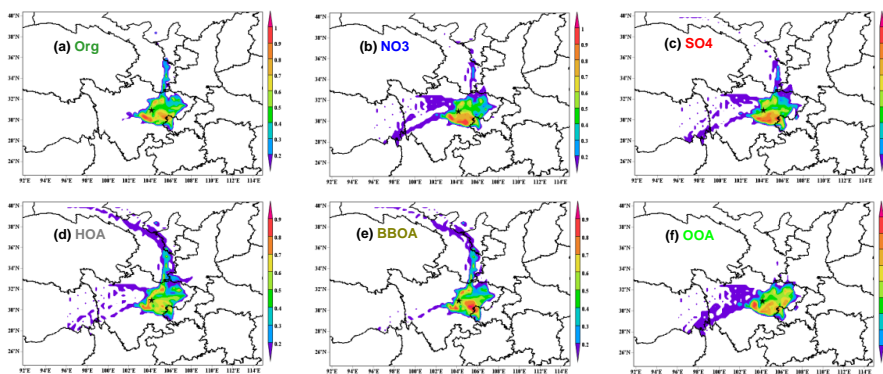
664 their transport paths.

665

666



667



668

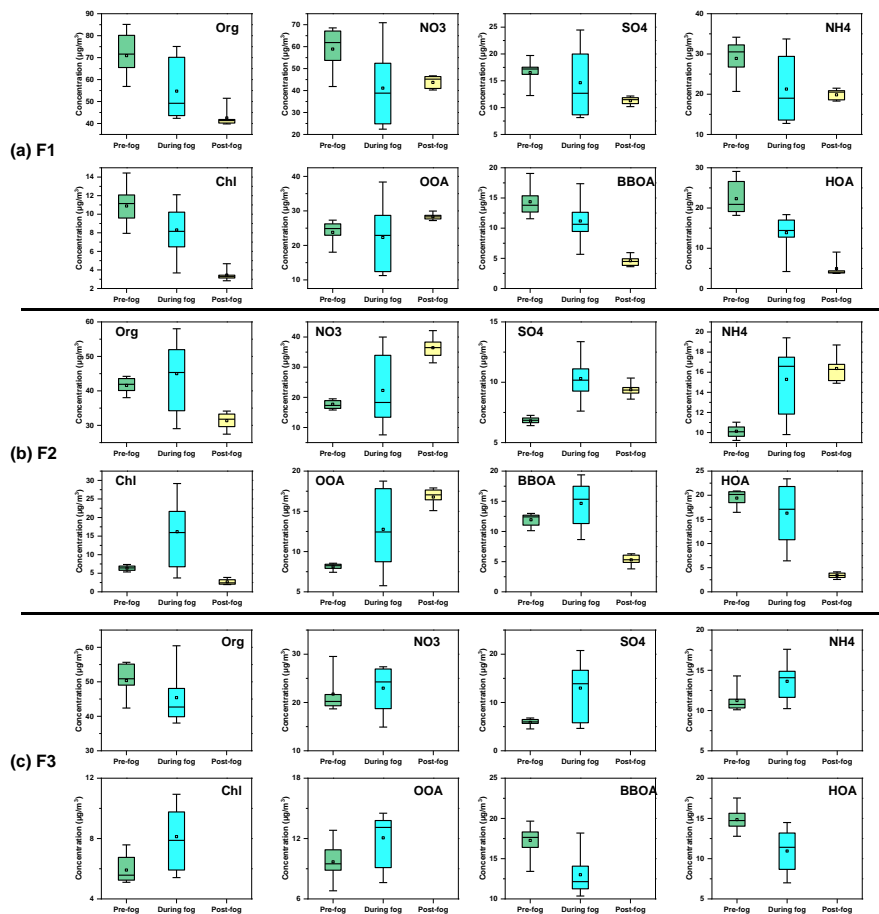
669 Fig. 12 Simulation results of PSCF for (a) organics, (b) nitrate, (c) sulphate, (d) HOA, (e) BBOA,
670 and (f) OOA during the whole campaign.

671

672



673



674

675 Fig. 13 Variation of organics, nitrate, sulphate, ammonium, chloride, OOA, BBOA, and HOA
676 concentration during the evolution of (a) F1, (b) F2, and (c) F3.

677

678



679

680 **References**

681

682 Aiken, A. C., Salcedo, D., Cubison, M. J., Huffman, J. A., DeCarlo, P. F., Ulbrich, I. M., Docherty, K.
683 S., Sueper, D., Kimmel, J. R., Worsnop, D. R., Trimborn, A., Northway, M., Stone, E. A., Schauer, J.
684 J., Volkamer, R. M., Fortner, E., de Foy, B., Wang, J., Laskin, A., Shutthanandan, V., Zheng, J.,
685 Zhang, R., Gaffney, J., Marley, N. A., Paredes-Miranda, G., Arnott, W. P., Molina, L. T., Sosa, G.,
686 and Jimenez, J. L.: Mexico City aerosol analysis during MILAGRO using high resolution aerosol
687 mass spectrometry at the urban supersite (T0) – Part 1: Fine particle composition and organic source
688 apportionment, *Atmos. Chem. Phys.*, 6633-6653, 2009.

689 Alfara, M. R., Prevot, A. S. H., Szidat, S., Sandradewi, J., Weimer, S., Lanz, V. A., Schreiber, D., Mohr,
690 M., and Baltensperger, U.: Identification of the Mass Spectral Signature of Organic Aerosols from
691 Wood Burning Emissions, *Environ. Sci. Technol.*, 41, 5770-5777, <https://doi.org/10.1021/es062289b>,
692 2007.

693 Bao, Z., Chen, L., Li, K., Han, L., Wu, X., Gao, X., Azzi, M., and Cen, K.: Meteorological and chemical
694 impacts on PM_{2.5} during a haze episode in a heavily polluted basin city of eastern China, *Environ.*
695 *Pollut.*, 250, 520-529, <https://doi.org/10.1016/j.envpol.2019.04.045>, 2019.

696 Boyd, C. M., Nah, T., Xu, L., Berkemeier, T., and Ng, N. L.: Secondary Organic Aerosol (SOA) from
697 Nitrate Radical Oxidation of Monoterpenes: Effects of Temperature, Dilution, and Humidity on
698 Aerosol Formation, Mixing, and Evaporation, *Environ. Sci. Technol.*, 51, 7831-7841,
699 <https://doi.org/10.1021/acs.est.7b01460>, 2017.

700 Chakraborty, A., Bhattu, D., Gupta, T., Tripathi, S. N., and Canagaratna, M. R.: Real-time measurements
701 of ambient aerosols in a polluted Indian city: Sources, characteristics, and processing of organic
702 aerosols during foggy and nonfoggy periods, *J. Geophys. Res.-Atmos.*, 120, 9006-9019,
703 <https://doi.org/10.1002/2015JD023419>, 2015.

704 Chakraborty, A., Gupta, T., and Tripathi, S. N.: Combined effects of organic aerosol loading and fog
705 processing on organic aerosols oxidation, composition, and evolution, *Sci. Total Environ.*, 573, 690-
706 698, <https://doi.org/10.1016/j.scitotenv.2016.08.156>, 2016.

707 Chantara, S., Thepnuan, D., Wiriya, W., Prawan, S., and Tsai, Y. I.: Emissions of pollutant gases, fine
708 particulate matters and their significant tracers from biomass burning in an open-system combustion



- 709 chamber, *Chemosphere*, 224, 407-416, <https://doi.org/10.1016/j.chemosphere.2019.02.153>, 2019.
- 710 Chen, Q., Fu, T., Hu, J., Ying, Q., and Zhang, L.: Modelling secondary organic aerosols in China, *Natl.*
711 *Sci. Rev.*, 4, 806-809, 2017.
- 712 Chen, Q., Heald, C. L., Jimenez, J. L., Canagaratna, M. R., Zhang, Q., He, L. Y., Huang, X. F.,
713 Campuzano Jost, P., Palm, B. B., Poulain, L., Kuwata, M., Martin, S. T., Abbatt, J. P. D., Lee, A. K.
714 Y., and Liggi, J.: Elemental composition of organic aerosol: The gap between ambient and laboratory
715 measurements, *Geophys. Res. Lett.*, 42, 4182-4189, <https://doi.org/10.1002/2015GL063693>, 2015.
- 716 Clark, C. H., Kacarab, M., Nakao, S., Asa-Awuku, A., Sato, K., and Cocker, D. R.: Temperature Effects
717 on Secondary Organic Aerosol (SOA) from the Dark Ozonolysis and Photo-Oxidation of Isoprene,
718 *Environ. Sci. Technol.*, 50, 5564-5571, <https://doi.org/10.1021/acs.est.5b05524>, 2016.
- 719 Collett, J. L., Herckes, P., Youngster, S., and Lee, T.: Processing of atmospheric organic matter by
720 California radiation fogs, *Atmos. Res.*, 87, 232-241, <https://doi.org/10.1016/j.atmosres.2007.11.005>,
721 2008.
- 722 Cubison, M. J., Ortega, A. M., Hayes, P. L., Farmer, D. K., Day, D., Lechner, M. J., Brune, W. H., Apel,
723 E., Diskin, G. S., Fisher, J. A., Fuelberg, H. E., Hecobian, A., Knapp, D. J., Mikoviny, T., Riemer, D.,
724 Sachse, G. W., Sessions, W., Weber, R. J., Weinheimer, A. J., Wisthaler, A., and Jimenez, J. L.:
725 Effects of aging on organic aerosol from open biomass burning smoke in aircraft and laboratory
726 studies, *Atmos. Chem. Phys.*, 11, 12049-12064, <https://doi.org/10.5194/acp-11-12049-2011>, 2011.
- 727 Dai, Q., Schulze, B. C., Bi, X., Bui, A. A. T., Guo, F., Wallace, H. W., Sanchez, N. P., Flynn, J. H., Lefer,
728 B. L., Feng, Y., and Griffin, R. J.: Seasonal differences in formation processes of oxidised organic
729 aerosol near Houston, TX, *Atmos. Chem. Phys.*, 19, 9641-9661, [https://doi.org/10.5194/acp-19-9641-](https://doi.org/10.5194/acp-19-9641-2019)
730 2019, 2019.
- 731 Ding, A., Huang, X., Nie, W., Chi, X., Xu, Z., Zheng, L., Xu, Z., Xie, Y., Qi, X., Shen, Y., Sun, P., Wang,
732 J., Wang, L., Sun, J., Yang, X., Qin, W., Zhang, X., Cheng, W., Liu, W., Pan, L., and Fu, C.:
733 Significant reduction of PM_{2.5} in eastern China due to regional-scale emission control: evidence from
734 SORPES in 2011-2018, *Atmos. Chem. Phys.*, 19, 11791-11801, [https://doi.org/10.5194/acp-19-](https://doi.org/10.5194/acp-19-11791-2019)
735 11791-2019, 2019.
- 736 Docherty, K. S., Corse, E. W., Jaoui, M., Offenberg, J. H., Kleindienst, T. E., Krug, J. D., Riedel, T. P.,
737 and Lewandowski, M.: Trends in the oxidation and relative volatility of chamber-generated secondary
738 organic aerosol, *Aerosol Sci. Tech.*, 52, 992-1004, <https://doi.org/10.1080/02786826.2018.1500014>,



- 739 2018.
- 740 Docherty, K. S., Stone, E. A., Ulbrich, I. M., DeCarlo, P. F., Snyder, D. C., Schauer, J. J., Peltier, R. E.,
741 Weber, R. J., Murphy, S. M., Seinfeld, J. H., Grover, B. D., Eatough, D. J., and Jimenez, J. L.:
742 Apportionment of Primary and Secondary Organic Aerosols in Southern California during the 2005
743 Study of Organic Aerosols in Riverside (SOAR-1), *Environ. Sci. Technol.*, 42, 7655-7662,
744 <https://doi.org/10.1021/es8008166>, 2008.
- 745 Donahue, N. M., Robinson, A. L., Stanier, C. O., and Pandis, S. N.: Coupled Partitioning, Dilution, and
746 Chemical Aging of Semivolatile Organics, *Environ. Sci. Technol.*, 40, 2635-2643,
747 <https://doi.org/10.1021/es052297c>, 2006.
- 748 Draxler, R. R., and Hess, G. D.: An overview of the HYSPLIT_4 modeling system for trajectories,
749 dispersion, and deposition, *Aust. Meteor. Mag.*, 47, 295-308, 1998.
- 750 Duan, J., Huang, R., Gu, Y., Lin, C., Zhong, H., Wang, Y., Yuan, W., Ni, H., Yang, L., Chen, Y.,
751 Worsnop, D. R., and O'Dowd, C.: The formation and evolution of secondary organic aerosol during
752 summer in Xi'an: Aqueous phase processing in fog-rain days, *Sci. Total Environ.*, 756, 144077,
753 <https://doi.org/10.1016/j.scitotenv.2020.144077>, 2021.
- 754 Fröhlich, R., Cubison, M. J., Slowik, J. G., Bukowiecki, N., Prévôt, A. S. H., Baltensperger, U.,
755 Schneider, J., Kimmel, J. R., Gonin, M., Rohner, U., Worsnop, D. R., and Jayne, J. T.: The ToF-
756 ACSM: a portable aerosol chemical speciation monitor with TOFMS detection, *Atmos. Meas. Tech.*,
757 6, 3225-3241, <https://doi.org/10.5194/amt-6-3225-2013>, 2013.
- 758 Fu, X., Wang, S., Xing, J., Zhang, X., Wang, T., and Hao, J.: Increasing Ammonia Concentrations
759 Reduce the Effectiveness of Particle Pollution Control Achieved via SO₂ and NO_x Emissions
760 Reduction in East China, *Environ. Sci. Technol. Lett.*, 4, 221-227,
761 <https://doi.org/10.1021/acs.estlett.7b00143>, 2017.
- 762 Fu, X., Wang, T., Gao, J., Wang, P., Liu, Y., Wang, S., Zhao, B., and Xue, L.: Persistent Heavy Winter
763 Nitrate Pollution Driven by Increased Photochemical Oxidants in Northern China, *Environ. Sci.*
764 *Technol.*, 54, 3881-3889, <https://doi.org/10.1021/acs.est.9b07248>, 2020.
- 765 Ge, D., Nie, W., Sun, P., Liu, Y., Wang, T., Wang, J., Wang, J., Wang, L., Zhu, C., Wang, R., Liu, T.,
766 Chi, X., and Ding, A.: Characterisation of particulate organic nitrates in the Yangtze River Delta, East
767 China, using the time-of-flight aerosol chemical speciation monitor, *Atmos. Environ.*, 272, 118927,
768 <https://doi.org/10.1016/j.atmosenv.2021.118927>, 2022.



- 769 Ge, X., Li, L., Chen, Y., Chen, H., Wu, D., Wang, J., Xie, X., Ge, S., Ye, Z., Xu, J., and Chen, M.:
770 Aerosol characteristics and sources in Yangzhou, China resolved by offline aerosol mass spectrometry
771 and other techniques, *Environ. Pollut.*, 225, 74-85, <https://doi.org/10.1016/j.envpol.2017.03.044>,
772 2017.
- 773 Gilardoni, S., Massoli, P., Paglione, M., Giulianelli, L., Carbone, C., Rinaldi, M., Decesari, S., Sandrini,
774 S., Costabile, F., Gobbi, G. P., Pietrogrande, M. C., Visentin, M., Scotto, F., Fuzzi, S., and Facchini,
775 M. C.: Direct observation of aqueous secondary organic aerosol from biomass-burning emissions, *P.*
776 *Natl. Acad. Sci. USA*, 113, 10013-10018, <https://doi.org/10.1073/pnas.1602212113>, 2016.
- 777 Guo, J., Zhou, S., Cai, M., Zhao, J., Song, W., Zhao, W., Hu, W., Sun, Y., He, Y., Yang, C., Xu, X.,
778 Zhang, Z., Cheng, P., Fan, Q., Hang, J., Fan, S., Wang, X., and Wang, X.: Characterisation of
779 submicron particles by time-of-flight aerosol chemical speciation monitor (ToF-ACSM) during
780 wintertime: aerosol composition, sources, and chemical processes in Guangzhou, China, *Atmos.*
781 *Chem. Phys.*, 20, 7595-7615, <https://doi.org/10.5194/acp-20-7595-2020>, 2020.
- 782 Guo, L., Guo, X., Fang, C., and Zhu, S.: Observation analysis on characteristics of formation, evolution
783 and transition of a long-lasting severe fog and haze episode in North China, *Sci. China Earth Sci.*, 58,
784 329-344, <https://doi.org/10.1007/s11430-014-4924-2>, 2015.
- 785 Guo, S., Hu, M., Zamora, M. L., Peng, J., Shang, D., Zheng, J., Du, Z., Wu, Z., Shao, M., Zeng, L.,
786 Molina, M. J., and Zhang, R.: Elucidating severe urban haze formation in China, *P. Natl. Acad. Sci.*
787 *USA*, 111, 17373-17378, <https://doi.org/10.1073/pnas.1419604111>, 2014.
- 788 He, K., Zhao, Q., Ma, Y., Duan, F., Yang, F., Shi, Z., and Chen, G.: Spatial and seasonal variability of
789 PM_{2.5} acidity at two Chinese megacities: insights into the formation of secondary inorganic aerosols,
790 *Atmos. Chem. Phys.*, 12, 1377-1395, <https://doi.org/10.5194/acp-12-1377-2012>, 2012.
- 791 Heald, C. L., Kroll, J. H., Jimenez, J. L., Docherty, K. S., DeCarlo, P. F., Aiken, A. C., Chen, Q., Martin,
792 S. T., Farmer, D. K., and Artaxo, P.: A simplified description of the evolution of organic aerosol
793 composition in the atmosphere, *Geophys. Res. Lett.*, 37, <https://doi.org/10.1029/2010GL042737>,
794 2010.
- 795 Herndon, S. C., Onasch, T. B., Wood, E. C., Kroll, J. H., Canagaratna, M. R., Jayne, J. T., Zavala, M.
796 A., Knighton, W. B., Mazzoleni, C., Dubey, M. K., Ulbrich, I. M., Jimenez, J. L., Seila, R., de Gouw,
797 J. A., de Foy, B., Fast, J., Molina, L. T., Kolb, C. E., and Worsnop, D. R.: Correlation of secondary
798 organic aerosol with odd oxygen in Mexico City, *Geophys. Res. Lett.*, 35,



- 799 <https://doi.org/10.1029/2008GL034058>, 2008.
- 800 Hinks, M. L., Montoya-Aguilera, J., Ellison, L., Lin, P., Laskin, A., Laskin, J., Shiraiwa, M., Dabdub,
801 D., and Nizkorodov, S. A.: Effect of relative humidity on the composition of secondary organic
802 aerosol from the oxidation of toluene, *Atmos. Chem. Phys.*, 18, 1643-1652,
803 <https://doi.org/10.5194/acp-18-1643-2018>, 2018.
- 804 Huang, R., Zhang, Y., Bozzetti, C., Ho, K., Cao, J., Han, Y., Daellenbach, K. R., Slowik, J. G., Platt, S.
805 M., Canonaco, F., Zotter, P., Wolf, R., Pieber, S. M., Bruns, E. A., Crippa, M., Ciarelli, G.,
806 Piazzalunga, A., Schwikowski, M., Abbaszade, G., Schnelle-Kreis, J., Zimmermann, R., An, Z.,
807 Szidat, S., Baltensperger, U., Haddad, I. E., and Prévôt, A. S. H.: High secondary aerosol contribution
808 to particulate pollution during haze events in China, *Nature*, 514, 218-222,
809 <https://doi.org/10.1038/nature13774>, 2014.
- 810 Huang, X., Zhang, J., Zhang, W., Tang, G., and Wang, Y.: Atmospheric ammonia and its effect on PM_{2.5}
811 pollution in urban Chengdu, Sichuan Basin, China, *Environ. Pollut.*, 291, 118195,
812 <https://doi.org/10.1016/j.envpol.2021.118195>, 2021.
- 813 Ianniello, A., Spataro, F., Esposito, G., Allegrini, I., Hu, M., and Zhu, T.: Chemical characteristics of
814 inorganic ammonium salts in PM_{2.5} in the atmosphere of Beijing (China), *Atmos. Chem. Phys.*, 11,
815 10803-10822, <https://doi.org/10.5194/acp-11-10803-2011>, 2011.
- 816 Izhar, S., Gupta, T., and Panday, A. K.: Scavenging efficiency of water soluble inorganic and organic
817 aerosols by fog droplets in the Indo Gangetic Plain, *Atmos. Res.*, 235, 104767,
818 <https://doi.org/10.1016/j.atmosres.2019.104767>, 2020.
- 819 Kim, H., Collier, S., Ge, X., Xu, J., Sun, Y., Jiang, W., Wang, Y., Herckes, P., and Zhang, Q.: Chemical
820 processing of water-soluble species and formation of secondary organic aerosol in fogs, *Atmos.*
821 *Environ.*, 200, 158-166, <https://doi.org/10.1016/j.atmosenv.2018.11.062>, 2019.
- 822 Kong, L., Tan, Q., Feng, M., Qu, Y., An, J., Liu, X., Cheng, N., Deng, Y., Zhai, R., and Wang, Z.:
823 Investigating the characteristics and source analyses of PM_{2.5} seasonal variations in Chengdu,
824 Southwest China, *Chemosphere*, 243, 125267, <https://doi.org/10.1016/j.chemosphere.2019.125267>,
825 2020.
- 826 Kuang, Y., He, Y., Xu, W., Yuan, B., Zhang, G., Ma, Z., Wu, C., Wang, C., Wang, S., Zhang, S., Tao,
827 J., Ma, N., Su, H., Cheng, Y., Shao, M., and Sun, Y.: Photochemical Aqueous-Phase Reactions Induce
828 Rapid Daytime Formation of Oxygenated Organic Aerosol on the North China Plain, *Environ. Sci.*



- 829 Technol., 54, 3849-3860, <https://doi.org/10.1021/acs.est.9b06836>, 2020.
- 830 Lanz, V. A., Alfarra, M. R., Baltensperger, U., Buchmann, B., Hueglin, C., and Prévôt, A. S. H.: Source
831 apportionment of submicron organic aerosols at an urban site by factor analytical modelling of aerosol
832 mass spectra, *Atmos. Chem. Phys.*, 7, 1503-1522, <https://doi.org/10.5194/acp-7-1503-2007>, 2007.
- 833 Li, H., Zhang, Q., Zheng, B., Chen, C., Wu, N., Guo, H., Zhang, Y., Zheng, Y., Li, X., and He, K.:
834 Nitrate-driven urban haze pollution during summertime over the North China Plain, *Atmos. Chem.*
835 *Phys.*, 18, 5293-5306, <https://doi.org/10.5194/acp-18-5293-2018>, 2018.
- 836 Liu, M., Huang, X., Song, Y., Xu, T., Wang, S., Wu, Z., Hu, M., Zhang, L., Zhang, Q., Pan, Y., Liu, X.,
837 and Zhu, T.: Rapid SO₂ emission reductions significantly increase tropospheric ammonia
838 concentrations over the North China Plain, *Atmos. Chem. Phys.*, 18, 17933-17943,
839 <https://doi.org/10.5194/acp-18-17933-2018>, 2018.
- 840 Liu, P. S. K., Deng, R., Smith, K. A., Williams, L. R., Jayne, J. T., Canagaratna, M. R., Moore, K.,
841 Onasch, T. B., Worsnop, D. R., and Deshler, T.: Transmission Efficiency of an Aerodynamic
842 Focusing Lens System: Comparison of Model Calculations and Laboratory Measurements for the
843 Aerodyne Aerosol Mass Spectrometer, *Aerosol Sci. Tech.*, 41, 721-733,
844 <https://doi.org/10.1080/02786820701422278>, 2007.
- 845 Liu, P., Ye, C., Xue, C., Zhang, C., Mu, Y., and Sun, X.: Formation mechanisms of atmospheric nitrate
846 and sulfate during the winter haze pollution periods in Beijing: gas-phase, heterogeneous and
847 aqueous-phase chemistry, *Atmos. Chem. Phys.*, 20, 4153-4165, [https://doi.org/10.5194/acp-20-4153-](https://doi.org/10.5194/acp-20-4153-2020)
848 2020, 2020.
- 849 Liu, T., Huang, D. D., Li, Z., Liu, Q., Chan, M., and Chan, C. K.: Comparison of secondary organic
850 aerosol formation from toluene on initially wet and dry ammonium sulfate particles at moderate
851 relative humidity, *Atmos. Chem. Phys.*, 18, 5677-5689, <https://doi.org/10.5194/acp-18-5677-2018>,
852 2018.
- 853 Man, H., Zhu, Y., Ji, F., Yao, X., Lau, N. T., Li, Y., Lee, B. P., and Chan, C. K.: Comparison of Daytime
854 and Nighttime New Particle Growth at the HKUST Supersite in Hong Kong, *Environ. Sci. Technol.*,
855 49, 7170-7178, <https://doi.org/10.1021/acs.est.5b02143>, 2015.
- 856 Mandariya, A. K., Gupta, T., and Tripathi, S. N.: Effect of aqueous-phase processing on the formation
857 and evolution of organic aerosol (OA) under different stages of fog life cycles, *Atmos. Environ.*, 206,
858 60-71, <https://doi.org/10.1016/j.atmosenv.2019.02.047>, 2019.



- 859 Matthew, B. M., Middlebrook, A. M., and Onasch, T. B.: Collection Efficiencies in an Aerodyne Aerosol
860 Mass Spectrometer as a Function of Particle Phase for Laboratory Generated Aerosols, *Aerosol Sci.*
861 *Tech.*, 42, 884-898, <https://doi.org/10.1080/02786820802356797>, 2008.
- 862 Middlebrook, A. M., Bahreini, R., Jimenez, J. L., and Canagaratna, M. R.: Evaluation of Composition-
863 Dependent Collection Efficiencies for the Aerodyne Aerosol Mass Spectrometer using Field Data,
864 *Aerosol Sci. Tech.*, 46, 258-271, <https://doi.org/10.1080/02786826.2011.620041>, 2012.
- 865 Mohr, C., DeCarlo, P. F., Heringa, M. F., Chirico, R., Slowik, J. G., Richter, R., Reche, C., Alastuey, A.,
866 Querol, X., Seco, R., Peñuelas, J., Jiménez, J. L., Crippa, M., Zimmermann, R., Baltensperger, U.,
867 and Prévôt, A. S. H.: Identification and quantification of organic aerosol from cooking and other
868 sources in Barcelona using aerosol mass spectrometer data, *Atmos. Chem. Phys.*, 12, 1649-1665,
869 <https://doi.org/10.5194/acp-12-1649-2012>, 2012.
- 870 Ng, N. L., Canagaratna, M. R., Jimenez, J. L., Chhabra, P. S., Seinfeld, J. H., and Worsnop, D. R.:
871 Changes in organic aerosol composition with aging inferred from aerosol mass spectra, *Atmos. Chem.*
872 *Phys.*, 11, 6465-6474, <https://doi.org/10.5194/acp-11-6465-2011>, 2011.
- 873 Ng, N. L., Canagaratna, M. R., Zhang, Q., Jimenez, J. L., Tian, J., Ulbrich, I. M., Kroll, J. H., Docherty,
874 K. S., Chhabra, P. S., Bahreini, R., Murphy, S. M., Seinfeld, J. H., Hildebrandt, L., Donahue, N. M.,
875 DeCarlo, P. F., Lanz, V. A., Prévôt, A. S. H., Dinar, E., Rudich, Y., and Worsnop, D. R.: Organic
876 aerosol components observed in Northern Hemispheric datasets from Aerosol Mass Spectrometry,
877 *Atmos. Chem. Phys.*, 10, 4625-4641, <https://doi.org/10.5194/acp-10-4625-2010>, 2010.
- 878 Ng, N. L., Herndon, S. C., Trimborn, A., Canagaratna, M. R., Croteau, P. L., Onasch, T. B., Sueper, D.,
879 Worsnop, D. R., Zhang, Q., Sun, Y. L., and Jayne, J. T.: An Aerosol Chemical Speciation Monitor
880 (ACSM) for Routine Monitoring of the Composition and Mass Concentrations of Ambient Aerosol,
881 *Aerosol Sci. Tech.*, 45, 780-794, <https://doi.org/10.1080/02786826.2011.560211>, 2011.
- 882 Paatero, P., and Tapper, U.: Positive matrix factorisation: A non-negative factor model with optimal
883 utilisation of error estimates of data values, *Environmetrics*, 5, 111-126, 1994.
- 884 Paglione, M., Gilardoni, S., Rinaldi, M., Decesari, S., Zanca, N., Sandrini, S., Giulianelli, L., Bacco, D.,
885 Ferrari, S., Poluzzi, V., Scotto, F., Trentini, A., Poulain, L., Herrmann, H., Wiedensohler, A.,
886 Canonaco, F., Prévôt, A. S. H., Massoli, P., Carbone, C., Facchini, M. C., and Fuzzi, S.: The impact
887 of biomass burning and aqueous-phase processing on air quality: a multi-year source apportionment
888 study in the Po Valley, Italy, *Atmos. Chem. Phys.*, 20, 1233-1254, <https://doi.org/10.5194/acp-20->



- 889 1233-2020, 2020.
- 890 Pathak, R. K., Wu, W. S., and Wang, T.: Summertime PM_{2.5} ionic species in four major cities of China:
891 nitrate formation in an ammonia-deficient atmosphere, *Atmos. Chem. Phys.*, 9, 1711-1722,
892 <https://doi.org/10.5194/acp-9-1711-2009>, 2009.
- 893 Peng, J., Hu, M., Shang, D., Wu, Z., Du, Z., Tan, T., Wang, Y., Zhang, F., and Zhang, R.: Explosive
894 Secondary Aerosol Formation during Severe Haze in the North China Plain, *Environ. Sci. Technol.*,
895 55, 2189-2207, <https://doi.org/10.1021/acs.est.0c07204>, 2021.
- 896 Polissar, A. V., Hopke, P. K., and Harris, J. M.: Source Regions for Atmospheric Aerosol Measured at
897 Barrow, Alaska, *Environ. Sci. Technol.*, 35, 4214-4226, <https://doi.org/10.1021/es0107529>, 2001.
- 898 Rollins, A. W., Browne, E. C., Min, K., Pusede, S. E., Wooldridge, P. J., Gentner, D. R., Goldstein, A.
899 H., Liu, S., Day, D. A., and Russell, L. M.: Evidence for NO_x control over nighttime SOA formation,
900 *Science*, 337, 1210-1212, 2012.
- 901 Song, M., Liu, X., Tan, Q., Feng, M., Qu, Y., An, J., and Zhang, Y.: Characteristics and formation
902 mechanism of persistent extreme haze pollution events in Chengdu, southwestern China, *Environ.*
903 *Pollut.*, 251, 1-12, <https://doi.org/10.1016/j.envpol.2019.04.081>, 2019.
- 904 Sun, Y. L., Zhang, Q., Anastasio, C., and Sun, J.: Insights into secondary organic aerosol formed via
905 aqueous-phase reactions of phenolic compounds based on high resolution mass spectrometry, *Atmos.*
906 *Chem. Phys.*, 10, 4809-4822, <https://doi.org/10.5194/acp-10-4809-2010>, 2010.
- 907 Sun, Y. L., Zhang, Q., Schwab, J. J., Demerjian, K. L., Chen, W. N., Bae, M. S., Hung, H. M., Hogrefe,
908 O., Frank, B., Rattigan, O. V., and Lin, Y. C.: Characterisation of the sources and processes of organic
909 and inorganic aerosols in New York city with a high-resolution time-of-flight aerosol mass
910 spectrometer, *Atmos. Chem. Phys.*, 11, 1581-1602, <https://doi.org/10.5194/acp-11-1581-2011>, 2011.
- 911 Sun, Y., Chen, C., Zhang, Y., Xu, W., Zhou, L., Cheng, X., Zheng, H., Ji, D., Li, J., Tang, X., Fu, P., and
912 Wang, Z.: Rapid formation and evolution of an extreme haze episode in Northern China during winter
913 2015, *Sci. Rep.-UK*, 6, <https://doi.org/10.1038/srep27151>, 2016.
- 914 Sun, Y., He, Y., Kuang, Y., Xu, W., Song, S., Ma, N., Tao, J., Cheng, P., Wu, C., Su, H., Cheng, Y., Xie,
915 C., Chen, C., Lei, L., Qiu, Y., Fu, P., Croteau, P., and Worsnop, D. R.: Chemical Differences Between
916 PM₁ and PM_{2.5} in Highly Polluted Environment and Implications in Air Pollution Studies, *Geophys.*
917 *Res. Lett.*, 47, <https://doi.org/10.1029/2019GL086288>, 2020.
- 918 Sun, Y., Jiang, Q., Xu, Y., Ma, Y., Zhang, Y., Liu, X., Li, W., Wang, F., Li, J., Wang, P., and Li, Z.:



919 Aerosol characterisation over the North China Plain: Haze life cycle and biomass burning impacts in
920 summer, *J. Geophys. Res.-Atmos.*, 121, 2508-2521, <https://doi.org/10.1002/2015JD024261>, 2016.

921 Tan, Z., Lu, K., Jiang, M., Su, R., Wang, H., Lou, S., Fu, Q., Zhai, C., Tan, Q., Yue, D., Chen, D., Wang,
922 Z., Xie, S., Zeng, L., and Zhang, Y.: Daytime atmospheric oxidation capacity in four Chinese
923 megacities during the photochemically polluted season: a case study based on box model simulation,
924 *Atmos. Chem. Phys.*, 19, 3493-3513, <https://doi.org/10.5194/acp-19-3493-2019>, 2019.

925 Tao, J., Zhang, L., Cao, J., and Zhang, R.: A review of current knowledge concerning PM_{2.5} chemical
926 composition, aerosol optical properties and their relationships across China, *Atmos. Chem. Phys.*, 17,
927 9485-9518, <https://doi.org/10.5194/acp-17-9485-2017>, 2017.

928 Tian, M., Liu, Y., Yang, F., Zhang, L., Peng, C., Chen, Y., Shi, G., Wang, H., Luo, B., Jiang, C., Li, B.,
929 Takeda, N., and Koizumi, K.: Increasing importance of nitrate formation for heavy aerosol pollution
930 in two megacities in Sichuan Basin, southwest China, *Environ. Pollut.*, 250, 898-905,
931 <https://doi.org/10.1016/j.envpol.2019.04.098>, 2019.

932 Ulbrich, I. M., Canagaratna, M. R., Zhang, Q., Worsnop, D. R., and Jimenez, J. L.: Interpretation of
933 organic components from Positive Matrix Factorization of aerosol mass spectrometric data, *Atmos.*
934 *Chem. Phys.*, 9, 2891-2918, 2009.

935 Vicente, A., Alves, C., Calvo, A. I., Fernandes, A. P., Nunes, T., Monteiro, C., Almeida, S. M., and Pio,
936 C.: Emission factors and detailed chemical composition of smoke particles from the 2010 wildfire
937 season, *Atmos. Environ.*, 71, 295-303, <https://doi.org/10.1016/j.atmosenv.2013.01.062>, 2013.

938 Wang, G., Zhang, R., Gomez, M. E., Yang, L., Levy Zamora, M., Hu, M., Lin, Y., Peng, J., Guo, S.,
939 Meng, J., Li, J., Cheng, C., Hu, T., Ren, Y., Wang, Y., Gao, J., Cao, J., An, Z., Zhou, W., Li, G.,
940 Wang, J., Tian, P., Marrero-Ortiz, W., Secret, J., Du, Z., Zheng, J., Shang, D., Zeng, L., Shao, M.,
941 Wang, W., Huang, Y., Wang, Y., Zhu, Y., Li, Y., Hu, J., Pan, B., Cai, L., Cheng, Y., Ji, Y., Zhang,
942 F., Rosenfeld, D., Liss, P. S., Duce, R. A., Kolb, C. E., and Molina, M. J.: Persistent sulfate formation
943 from London Fog to Chinese haze, *P. Natl. Acad. Sci. USA*, 113, 13630-13635,
944 <https://doi.org/10.1073/pnas.1616540113>, 2016.

945 Wang, H., Tian, M., Chen, Y., Shi, G., Liu, Y., Yang, F., Zhang, L., Deng, L., Yu, J., Peng, C., and Cao,
946 X.: Seasonal characteristics, formation mechanisms and source origins of PM_{2.5} in two megacities in
947 Sichuan Basin, China, *Atmos. Chem. Phys.*, 18, 865-881, <https://doi.org/10.5194/acp-18-865-2018>,
948 2018.



- 949 Wang, J., Ge, X., Chen, Y., Shen, Y., Zhang, Q., Sun, Y., Xu, J., Ge, S., Yu, H., and Chen, M.: Highly
950 time-resolved urban aerosol characteristics during springtime in Yangtze River Delta, China: insights
951 from soot particle aerosol mass spectrometry, *Atmos. Chem. Phys.*, 16, 9109-9127,
952 <https://doi.org/10.5194/acp-16-9109-2016>, 2016.
- 953 Wang, J., Li, J., Ye, J., Zhao, J., Wu, Y., Hu, J., Liu, D., Nie, D., Shen, F., Huang, X., Huang, D. D., Ji,
954 D., Sun, X., Xu, W., Guo, J., Song, S., Qin, Y., Liu, P., Turner, J. R., Lee, H. C., Hwang, S., Liao, H.,
955 Martin, S. T., Zhang, Q., Chen, M., Sun, Y., Ge, X., and Jacob, D. J.: Fast sulfate formation from
956 oxidation of SO₂ by NO₂ and HONO observed in Beijing haze, *Nat. Commun.*, 11,
957 <https://doi.org/10.1038/s41467-020-16683-x>, 2020.
- 958 Wang, J., Ye, J., Zhang, Q., Zhao, J., Wu, Y., Li, J., Liu, D., Li, W., Zhang, Y., Wu, C., Xie, C., Qin, Y.,
959 Lei, Y., Huang, X., Guo, J., Liu, P., Fu, P., Li, Y., Lee, H. C., Choi, H., Zhang, J., Liao, H., Chen, M.,
960 Sun, Y., Ge, X., Martin, S. T., and Jacob, D. J.: Aqueous production of secondary organic aerosol
961 from fossil-fuel emissions in winter Beijing haze, *P. Natl. Acad. Sci. USA*, 118,
962 <https://doi.org/10.1073/pnas.2022179118>, 2021.
- 963 Wang, Y., Yao, L., Wang, L., Liu, Z., Ji, D., Tang, G., Zhang, J., Sun, Y., Hu, B., and Xin, J.: Mechanism
964 for the formation of the January 2013 heavy haze pollution episode over central and eastern China,
965 *Sci. China Earth Sci.*, 57, 14-25, <https://doi.org/10.1007/s11430-013-4773-4>, 2014.
- 966 Weber, R. J., Guo, H., Russell, A. G., and Nenes, A.: High aerosol acidity despite declining atmospheric
967 sulfate concentrations over the past 15 years, *Nat. Geosci.*, 9, 282-285,
968 <https://doi.org/10.1038/ngeo2665>, 2016.
- 969 Weimer, S., Alfarra, M. R., Schreiber, D., Mohr, M., Prévôt, A. S. H., and Baltensperger, U.: Organic
970 aerosol mass spectral signatures from wood-burning emissions: Influence of burning conditions and
971 wood type, *J. Geophys. Res.*, 113, <https://doi.org/10.1029/2007JD009309>, 2008.
- 972 Wen, L., Xue, L., Wang, X., Xu, C., Chen, T., Yang, L., Wang, T., Zhang, Q., and Wang, W.:
973 Summertime fine particulate nitrate pollution in the North China Plain: increasing trends, formation
974 mechanisms and implications for control policy, *Atmos. Chem. Phys.*, 18, 11261-11275,
975 <https://doi.org/10.5194/acp-18-11261-2018>, 2018.
- 976 Wu, L., Zhang, X., Sun, J., Wang, Y., Zhong, J., and Meng, Z.: Intensified wintertime secondary
977 inorganic aerosol formation during heavy haze pollution episodes (HPEs) in Beijing, China, *J.*
978 *Environ. Sci.-China*, <https://doi.org/10.1016/j.jes.2022.01.008>, 2022.



- 979 Xu, W., Croteau, P., Williams, L., Canagaratna, M., Onasch, T., Cross, E., Zhang, X., Robinson, W.,
980 Worsnop, D., and Jayne, J.: Laboratory characterisation of an aerosol chemical speciation monitor
981 with PM_{2.5} measurement capability, *Aerosol Sci. Tech.*, 51, 69-83, 2017.
- 982 Xu, W., Han, T., Du, W., Wang, Q., Chen, C., Zhao, J., Zhang, Y., Li, J., Fu, P., Wang, Z., Worsnop, D.
983 R., and Sun, Y.: Effects of Aqueous-Phase and Photochemical Processing on Secondary Organic
984 Aerosol Formation and Evolution in Beijing, China, *Environ. Sci. Technol.*, 51, 762-770,
985 <https://doi.org/10.1021/acs.est.6b04498>, 2017.
- 986 Yan, F., Chen, W., Jia, S., Zhong, B., Yang, L., Mao, J., Chang, M., Shao, M., Yuan, B., Situ, S., Wang,
987 X., Chen, D., and Wang, X.: Stabilisation for the secondary species contribution to PM_{2.5} in the Pearl
988 River Delta (PRD) over the past decade, China: A meta-analysis, *Atmos. Environ.*, 242, 117817,
989 <https://doi.org/10.1016/j.atmosenv.2020.117817>, 2020.
- 990 Yu, L., Smith, J., Laskin, A., Anastasio, C., Laskin, J., and Zhang, Q.: Chemical characterisation of SOA
991 formed from aqueous-phase reactions of phenols with the triplet excited state of carbonyl and
992 hydroxyl radical, *Atmos. Chem. Phys.*, 14, 13801-13816, <https://doi.org/10.5194/acp-14-13801-2014>,
993 2014.
- 994 Zhai, S., Jacob, D. J., Wang, X., Liu, Z., Wen, T., Shah, V., Li, K., Moch, J. M., Bates, K. H., Song, S.,
995 Shen, L., Zhang, Y., Luo, G., Yu, F., Sun, Y., Wang, L., Qi, M., Tao, J., Gui, K., Xu, H., Zhang, Q.,
996 Zhao, T., Wang, Y., Lee, H. C., Choi, H., and Liao, H.: Control of particulate nitrate air pollution in
997 China, *Nat. Geosci.*, 14, 389-395, <https://doi.org/10.1038/s41561-021-00726-z>, 2021.
- 998 Zhan, B., Zhong, H., Chen, H., Chen, Y., Li, X., Wang, L., Wang, X., Mu, Y., Huang, R., George, C.,
999 and Chen, J.: The roles of aqueous-phase chemistry and photochemical oxidation in oxygenated
1000 organic aerosols formation, *Atmos. Environ.*, 266, 118738,
1001 <https://doi.org/10.1016/j.atmosenv.2021.118738>, 2021.
- 1002 Zhang, L., Guo, X., Zhao, T., Gong, S., Xu, X., Li, Y., Luo, L., Gui, K., Wang, H., Zheng, Y., and Yin,
1003 X.: A modelling study of the terrain effects on haze pollution in the Sichuan Basin, *Atmos. Environ.*,
1004 196, 77-85, <https://doi.org/10.1016/j.atmosenv.2018.10.007>, 2019.
- 1005 Zhang, Q., Jimenez, J. L., Canagaratna, M. R., Ulbrich, I. M., Ng, N. L., Worsnop, D. R., and Sun, Y.:
1006 Understanding atmospheric organic aerosols via factor analysis of aerosol mass spectrometry: a
1007 review, *Anal. Bioanal. Chem.*, 401, 3045-3067, <https://doi.org/10.1007/s00216-011-5355-y>, 2011.
- 1008 Zhang, Q., Worsnop, D. R., Canagaratna, M. R., and Jimenez, J. L.: Hydrocarbon-like and oxygenated



- 1009 organic aerosols in Pittsburgh: insights into sources and processes of organic aerosols, *Atmos. Chem.*
1010 *Phys.*, 5, 3289-3311, <https://doi.org/10.5194/acp-5-3289-2005>, 2005.
- 1011 Zhang, Y. W., Zhang, X. Y., Zhang, Y. M., Shen, X. J., Sun, J. Y., Ma, Q. L., Yu, X. M., Zhu, J. L.,
1012 Zhang, L., and Che, H. C.: Significant concentration changes of chemical components of PM₁ in the
1013 Yangtze River Delta area of China and the implications for the formation mechanism of heavy haze–
1014 fog pollution, *Sci. Total Environ.*, 538, 7-15, <https://doi.org/10.1016/j.scitotenv.2015.06.104>, 2015.
- 1015 Zhao, D., Liu, G., Xin, J., Quan, J., Wang, Y., Wang, X., Dai, L., Gao, W., Tang, G., Hu, B., Ma, Y.,
1016 Wu, X., Wang, L., Liu, Z., and Wu, F.: Haze pollution under a high atmospheric oxidation capacity
1017 in summer in Beijing: insights into formation mechanism of atmospheric physicochemical processes,
1018 *Atmos. Chem. Phys.*, 20, 4575-4592, <https://doi.org/10.5194/acp-20-4575-2020>, 2020.
- 1019 Zhao, J., Qiu, Y., Zhou, W., Xu, W., Wang, J., Zhang, Y., Li, L., Xie, C., Wang, Q., Du, W., Worsnop,
1020 D. R., Canagaratna, M. R., Zhou, L., Ge, X., Fu, P., Li, J., Wang, Z., Donahue, N. M., and Sun, Y.:
1021 Organic Aerosol Processing During Winter Severe Haze Episodes in Beijing, *J. Geophys. Res.-*
1022 *Atmos.*, 124, 10248-10263, <https://doi.org/10.1029/2019JD030832>, 2019.
- 1023 Zhao, R., Mungall, E. L., Lee, A. K. Y., Aljawhary, D., and Abbatt, J. P. D.: Aqueous-phase
1024 photooxidation of levoglucosan – a mechanistic study using aerosol time-of-flight chemical ionisation
1025 mass spectrometry (Aerosol ToF-CIMS), *Atmos. Chem. Phys.*, 14, 9695-9706,
1026 <https://doi.org/10.5194/acp-14-9695-2014>, 2014.
- 1027 Zheng, G. J., Duan, F. K., Su, H., Ma, Y. L., Cheng, Y., Zheng, B., Zhang, Q., Huang, T., Kimoto, T.,
1028 Chang, D., Pöschl, U., Cheng, Y. F., and He, K. B.: Exploring the severe winter haze in Beijing: the
1029 impact of synoptic weather, regional transport and heterogeneous reactions, *Atmos. Chem. Phys.*, 15,
1030 2969-2983, <https://doi.org/10.5194/acp-15-2969-2015>, 2015.
- 1031 Zheng, G., Duan, F., Ma, Y., Zhang, Q., Huang, T., Kimoto, T., Cheng, Y., Su, H., and He, K.: Episode-
1032 Based Evolution Pattern Analysis of Haze Pollution: Method Development and Results from Beijing,
1033 China, *Environ. Sci. Technol.*, 50, 4632-4641, <https://doi.org/10.1021/acs.est.5b05593>, 2016.
- 1034 Zhou, W., Chen, C., Lei, L., Fu, P., and Sun, Y.: Temporal variations and spatial distributions of gaseous
1035 and particulate air pollutants and their health risks during 2015–2019 in China, *Environ. Pollut.*, 272,
1036 116031, <https://doi.org/10.1016/j.envpol.2020.116031>, 2021.
- 1037